# Isovalent substitution in metal chalcogenide materials for improving thermoelectric power generation – A critical review

Jamal-Deen Musah[1,2], A. M. Ilyas[3,4], Shishir Venkatesh[1], Solomon Mensah[5], Samuel Kwofie[6], Vellaisamy A. L. Roy[7] (✉), and Chi-Man Lawrence Wu[1] (✉)

[1] Department of Materials Science and Engineering, City University of Hong Kong, Kowloon, Hong Kong, China

[2] Department of Electrical Engineering, The Hong Kong Polytechnic University, Hong Kong, China

[3] Department of Physics, City University of Hong Kong, Kowloon, Hong Kong, China

[4] Hong Kong Centre for Cerebro-Cardiovascular Health Engineering (COCHE), Hong Kong, China

[5] Department of Computer Science, University of Ghana, Legon, Accra, Ghana

[6] Department of Materials Engineering, Kwame Nkrumah University of Science and Technology (KNUST), Kumasi, Ghana

[7] James Watt School of Engineering, University of Glasgow, Glasgow G128QQ, UK

## ABSTRACT

The adverse effect of fossil fuels on the environment is driving research to explore alternative energy sources. Research studies have demonstrated that renewables can offer a promising strategy to curb the problem, among which thermoelectric technology stands tall. However, the challenge with thermoelectric materials comes from the conflicting property of the Seebeck coefficient and the electrical conductivity resulting in a low power factor and hence a lower figure of merit. Researchers have reported various techniques to enhance the figure of merit, particularly in metal chalcogenide thermoelectric materials. Here we present a review on isovalent substitution as a tool to decouple the interdependency of the electrical conductivity and Seebeck coefficient to facilitate simultaneous enhancement in these two parameters. This is proven true in both cationic and anionic side substitutions in metal chalcogenide thermoelectric materials. Numerous publications relating to isovalent substitution in metal chalcogenide thermoelectric are reviewed. This will serve as a direction for current and future research to enhance thermoelectric performance and device application. This review substantiates the role of isovalent substitution in enhancing metal chalcogenide thermoelectric properties compared with conventional systems.

## 1    Introduction

Energy generation is likely to be the foremost scientific challenge in the years to come. This is due to the globally increased demand for energy partly due to the uncontrollable rise in population. This has spurred the search for alternative means of power generation. Moreover, rampant global climate change due to fossil fuel combustion has prompted the research community to eradicate this menace by providing an alternative means of generating energy, which operates without contamination to the environment. Using theoretical calculation, Cullen et al. [1] established that, provided all energy conversion devices operate at their respective maximum efficiency, the global energy demand could be reduced by 90%. Similarly, 90% of the energy consumed by human activities is generated by the thermal process, which eventually is dissipated as heat [2]. Thermoelectric (TE) technology offers the best avenue of directly generating electricity from waste heat [3–5]. This approach provides a solution to climate and environmental problems while broadening our energy resources.

Thermoelectric device performance is quantified by the dimensionless parameter ($zT$), which is defined as $zT = [\mathrm{PF}/(\kappa_e + \kappa_l)]T$, where PF is the power factor, $\kappa_l$ and $\kappa_e$ are the lattices and electronic thermal conductivities, respectively, $T$ is the temperature whilst PF is the thermoelectric power factor which is defined as $\mathrm{PF} = S^2\sigma$, with $\sigma$ being the electrical conductivity and $S$ as the Seebeck coefficient. The figure of merit of any material that contributes to the efficiency of energy conversion of thermoelectric devices for both heating and cooling systems can be well described by the coefficient of performance (COP) [6], where the COP requires correspondingly high zT of the TE materials. Details of the COP is presented in section 2.

It is important to mention that the COP of thermoelectric

Address correspondence to Chi-Man Lawrence Wu, lawrence.wu@cityu.edu.hk; Vellaisamy A.L. Roy, Roy.vellaisamy@glasgow.ac.uk

refrigerators is linked with the zT of the TE material. The zT of the state-of-the-art $Bi_2Te_3$ materials (zT ~ 0.8) is enough to produce a COP of 10 K. Irrespective of the low COP, TE coolers can yield a high cooling temperature. A proper material design can enhance the zT of TE materials, which will improve the COP. The $\sigma$ is directly dependent on the carrier concentration and mobility. Enhancing carrier concentration enhances the $\sigma$ and decreases the Seebeck coefficient, which reduces the power factor. Ideally, for achieving a high zT, every thermoelectric material requires simultaneous enhancement in the electrical conductivity and Seebeck coefficient coupled with a decrease in the total thermal conductivity. However, due to the effective coupling of these parameters, it is challenging to increase both $\sigma$ and $S$ and decrease the total thermal conductivity ($\kappa_T$). This is due to the interdependency among these parameters. Due to the difficulty in simultaneously enhancing two or more thermoelectric properties, several studies focus on drastically decreasing the lattice thermal conductivity via enhanced phonon scattering mechanisms without deteriorating the power factor.

Developing newly improved functional materials for harvesting energy that does not threaten the environment is vital for the next generation. Unlike conventional energy harvesters, TE device technology is reliable, scalable, economical and environmentally friendly. Thermoelectric devices are exceptional as they do not involve moving parts [7]. This makes TE technology maintenance-free. Areas of application where TE immediately replaces the conventional power generators are long term low power sensors, wearable electronics, and wireless sensor networks.

The past few decades earmarked the first generation of bulk thermoelectric materials. These materials exhibited an efficiency of about 5%–6% and a thermoelectric figure of merit of about 0.8–1.0 [8]. Most of these materials, which saw the light of the day for practical usage, fall under the metal chalcogenides (MC) class, among which the most recognized state-of-the-art TE material for room temperature TE application is $Bi_2Te_3$ [9]. Researchers have published several reviews on strategies to improve TE performance, including band engineering of thermoelectric materials [10], synthesis of chalcogenides [11], wearable thermoelectric power generation [12], nanostructured thermoelectric materials [12, 13], oxides [14], and sulfides [15, 16]. However, there has not been any review paper on the effect of an isovalent substitution on MC as a TE material. Studies have shown that isovalent substitution in MCs can simultaneously enhance the power factor while diminishing thermal conductivity by forming resonant states.

This review covers the emerging mechanism of enhancing MC thermoelectric performance through isovalent substitution. MC compounds are typically seen as $M_2C_3$, where (M = metal and C = chalcogen). The substitution of a different metal for "M" or a second chalcogen for "C", which are of equal valence number as those of "M" and "C", respectively, have proven to be a salient way of enhancing the performance of TE properties in MC. Introduction to the start-of-the-art thermoelectric materials and devices is shown in Section 1. Section 2 presents the general description of thermoelectric power generation, analysis of the Landuer-Boltzman approach to thermoelectric properties, and derivation of TE transport properties. Section 3 discusses the recent advancement of isovalent substitution in metal chalcogenide materials for TE application. Sections 4 and 5 provide the threats to the validity of this study and the conclusion, respectively.

## 2 General description of thermoelectric power generation

Thermoelectric power generation involves converting waste thermal energy (heat) into usable electric power. This energy recovery process from heat to electricity is not a new phenomenon but was discovered in 1822 by a German Scientist, Thomas Seebeck. He observed an electrical voltage generated when two dissimilar but electrically conducting materials are connected in a closed circuit with a temperature gradient. The effect is termed the Seebeck effect, and the two junctions are termed the thermoelectric couples. In a typical design of a TE module, the p-type and the n-type legs of the modules are connected electrically in series and thermally in parallel. This is then sandwiched between thermally conducting plates. The physical explanation of thermoelectricity is due to the difference in the thermal energy of mobile charge carriers (electrons and holes) at the cold and the hot end. The heat transported from the hot side to the cold end is accomplished by the diffusion of energised charge carriers from the hot side to the cold end. This leads to an inhomogeneous charge distribution due to the larger number of charge carriers at the cold end than the hot end. It, therefore, creates an electric field, which opposes the diffusion process. Similarly, the accumulation of negatively charged carriers at the cold end renders it the negative terminal while the hot end becomes a positive terminal. Considering an open circuit condition, the rate of diffusion of the carriers from the hot end to the cold balances the electric field effect due to the charge movement from the cold to the hot end and leads to a state of equilibrium. Hence, the formation of the electrochemical potential ($\mu$) is measured as the Seebeck voltage response to the temperature gradient. Accordingly, the overall voltage generated per unit temperature gradient is referred to as the Seebeck coefficient. For a closed circuit, the electrochemical potential via the Seebeck voltage drives current through the circuit to serve as the electric power. More importantly, since electrons and holes have a different directions of movement, the overall current generated does not counteract but accumulates. This is a fundamental process for thermoelectric power generation [3, 6, 17].

Figure 1(a) is a typical thermoelectric device, and Fig. 1(b) shows how the n-type and p-type legs of a thermoelectric device are designed, thus explaining the direction of the flow of current through each leg. The thermal conductivity of TE materials cannot be reduced beyond the amorphous limit due to the phonon mean free path being limited by interatomic distance except in cases of nanostructuring [20]. It, therefore, becomes significant to couple the thermal conductivity reduction with thermoelectric power factor enhancement to realise the very high TE performance.

The recent advancement in thermoelectric material performance has seen its utilization in device fabrication, whereby thermal waste heat is converted into valuable electrical energy. Therefore, the conversion of heat flux into electrical power or vice versa is utilized by a thermoelectric generator (TEG) or thermoelectric cooler (TEC), where there is always a coupling of the transport between electrons and phonons. Maximum output power density ($\eta_{max}$) and heat to power conversion efficiency ($\eta_{max}$) of TE devices are expressed as:
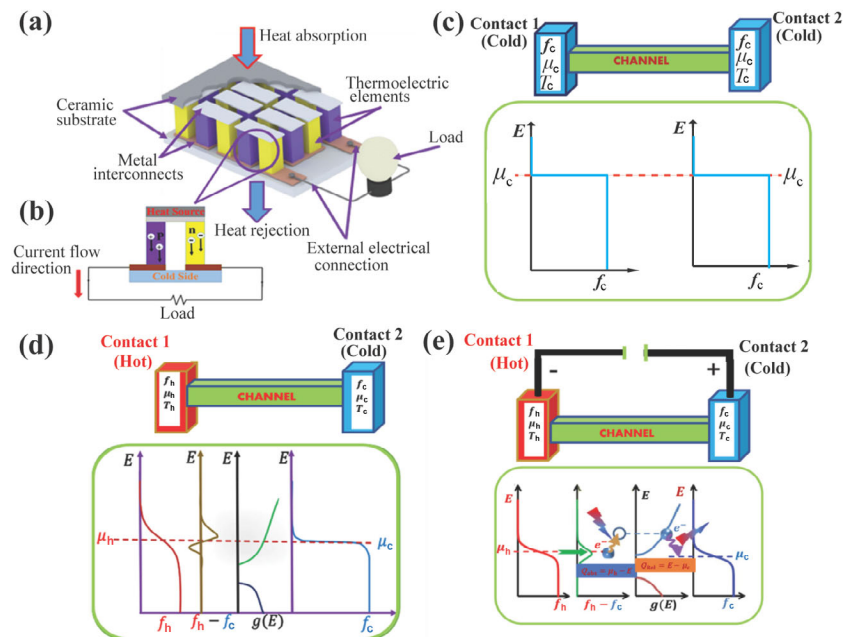
**Figure 1** (a) A typical thermoelectric device. (b) A TE n-type and p-type legs in the device design. Adapted with permission from Ref. [19], © WILEY-VCH Verlag GmbH & Co. KGaA, Weinheim 2017. (c) Initial stage of a thermoelectric device with no applied potential and temperature. (d) A TE device with temperature gradient leading to current flow due to difference in electrochemical potential ( $\mu_h \neq \mu_c$ ). (e) Peltier device with charge current driven by the applied potential. Adapted with permission from Ref. [116], © IOP Science 2018.

$$\eta_{max} = n_C \left[ \frac{\sqrt{zT+1} - 1}{\sqrt{zT+1} + \dfrac{T_c}{T_h}} \right] \quad (1)$$

$$n_C = \frac{T_h - T_c}{T_h} \quad (2)$$

$$\delta_{max} = \frac{(T_h - T_c)^2}{4L} PF \quad (3)$$

where $T_c$, $T_h$, $zT$, $L$, and PF are the cold end temperature, hot end temperature, average materials figure of merit, length of the device, and power factor, respectively.

It is evident from Eq. (3) that the PF value is significant in power generation applications linked with the TE output power density. Thermoelectric device efficiency is the ratio of the electrical power generated and the rate of heat directed through the thermoelectric module.

Again the efficiency of the cooling TE device is characterized by the COP [21, 22].

$$COP = \frac{T_c}{T_h - T_c} \frac{\sqrt{1 + z\overline{T}} - {T_c}/{T_h}}{\sqrt{1 + z\overline{T}} + 1} \quad (4)$$

The $\eta_{max}$ and $\eta_{max}$ relations show a function of zT, and average temperature ($\overline{T}$), which implies that a higher zT corresponds to improved power generation and cooling. The TE phenomena are highly realistic and reliable because of their solid-state nature, which means no moving part is involved, making the device friction-free, lightweight, quiet in operation, and scalable. The thermoelectric device (TED) can be switched from TEG to TEC by adjusting the direction of the current flow. This is a boost for harnessing energy with minimal emission of greenhouse gases. TED has vast areas of potential applications [23], including human body heat harvesting [23],

fossil-fuel power stations [19], jet engines, portable camping stoves, gas pipelines [24], etc. An estimated zT of at least 1.5 is enough to promote significant power generation [25]. However, till now, the most performing TE devices have an average zT of less than unity. This has limited TE devices to niche application areas, such as space probes because performance is less important than reliability [19]. Yuan et al. [26] fabricated a TEG based on a p-type ($Bi_{0.5}Sb_{1.5}Te_3$) and n-type ($Bi_2Te_{2.8}Se_{0.2}$) using a polyimide substrate. Then, 5 μm thin waterproof perylene thin film was used to encapsulate the device.

A maximum power density and power of 3 μW·cm$^{-2}$ and 190 μW, respectively, was achieved at a temperature change of 14 K with a corresponding output voltage of 40 mV. Similarly, Yuan et al. [27] deployed the same materials to fabricate a TEG multi-sensory device to monitor the small changes in skin humidity, temperature, and human activity. Measuring the human wrist, an output voltage between 2.8 and 3.3 V was achieved with a power density of 3.5 μW·cm$^{-2}$. Again, a chargeless and stand-alone sensor was made of $Bi_2Se_{0.3}Te_{2.7}$ and p-type $Bi_{0.5}Sb_{1.5}Te_3$ TEG by Kim et al. [28]. This device produced an output voltage, power, and power density of 10 mV, 83 μW, and 8.7 μW·cm$^{-2}$, respectively. For a TEG to be used as a battery, an output voltage of 1.5 V is required. The generated voltage, in this case, requires a voltage booster to produce a voltage up to 3.7 V for the TEG to be used as a glucose sensor. A flexible TEG device made from silicone rubber substrate using n-type $Bi_2Te_3$ and p-type $Bi_{0.3}Sb_{1.7}Te_3$ materials was fabricated by Toan et al. [29]. An output voltage of 1 V was realized at a temperature difference of 333 K. its maximum power and power density produced by this device under the same condition are 77.41 μW and 552.9 μW·cm$^{-2}$, respectively. The device's flexibility, mechanical stability, and TE performance show the possibility of its usage as an electrical power source for humidity temperature monitoring devices. The device's high performance can be attributed to the high thermoelectric properties of the n-type and p-type modules.

Eqations (1) to (4) show that for a given temperature difference $(\Delta T)$, $\Delta T = T_h - T_c$, the thermoelectric efficiency is determined by the figure of merit of the device. However, zT has two conflicting material properties. zT is directly proportional to the electrical conductivity and inversely proportional to the thermal conductivity. More so, several known best electrical conductors, are also good thermal conductors. Therefore, it is challenging to simultaneously increase electrical conductivity and decrease thermal conductivity to satisfy the zT enhancement relation, which is the main reason behind the low efficiencies of thermoelectric generators and refrigerators. Commercially available thermoelectric modules give an efficiency of 0.1%–8% [30]. For instance, Bi$_2$Te$_3$ with zT of 0.7 provides efficiency of 0.18%. This is calculated using Eq. (20). The low efficiency emerges as a problem, especially during low-temperature difference operation. Due to this low efficiency, TE devices still require enhancement. Isovalent substitution is a technique for enhancing electrical conductivity and Seebeck coefficient with low thermal conductivity.

## 2.1 Landauer-Boltzmann approach to thermoelectric properties

The Landauer-Boltzmann approximation is essential to determine a thermoelectric device's conductance, charge current, and heat current. Figure 1(c) depicts a single thermoelectric leg with two metal contacts and a channel. Each contact is defined by a Fermi function and electrochemical potential $f$ and $\mu$, respectively, assuming a very small device. At equilibrium, there is a common electrochemical potential $(\mu_h = \mu_c)$, as shown in Fig. 1(c). This implies that all energy states below it are occupied, whereas all energy states above are empty. This is the case at zero temperature. However, at non-zero temperature, as shown in Fig. 1(d), the distribution of electrons is described by the Fermi distribution function $(f_0)$ defined in Eq. (5) [31], viz,

$$f_0(E) = \frac{1}{\exp\left[\dfrac{E - \mu}{K_B T}\right] + 1} \tag{5}$$

where $E$ is the electron energy level, $\mu$ is the chemical potential, $K_B$ is the Boltzmann's constant, and $T$ the temperature. This function is always zero and unity, far above and far below the electrochemical potential, respectively. This brings about a difference in the electrochemical potential, $\mu_h \neq \mu_c$. Transition, therefore, occurs at the Fermi window of energy ranges of a few orders of $K_B T$. It could be deduced that, $f_0 = 0$ for $E >> \mu$ and for $E << \mu$, $f_0 = 1$. It is worth noting that, at non-zero temperature, $K$, the transition of $f_0$ from 0–1 occurs over an energy window of several $K_B T$ while at zero temperature, the transition of f$_0$ from 0–1 occurs exactly at $\mu$. External potential and temperature applied to a given material could alter the distribution of charge carriers. This implies that the Fermi distribution function is governed by temperature and the chemical potential at a specific energy, $E$ (Eq. 5). This difference in the electrochemical potential leads to the current flow.

From Fig. 1(c), when the temperatures of the two contacts are equal, $T_h = T_c$, and no external potential is applied, the electrochemical potential remain the same, and no charge is transported from one terminal to the other; hence no current is recorded $(I = 0)$.

However, when a temperature gradient is created between the two contacts (Fig. 1(d)) or an external voltage is applied to the terminals (Fig. 1(e)), there is a change in the electrochemical potentials at the two terminals. This results in $T_h - T_c \neq 0$, $\mu_h - \mu_c \neq 0$ and therefore creates a difference in the Fermi function $(f_h \neq f_c)$. Therefore, the difference in the Fermi distribution function due to the difference in temperature or the applied voltage leads to current flow through the device around the electrochemical potential.

It is worth mentioning that only electrons with energies greater than the chemical potential flow from the hot contact to the cold contact, while charges with energies less than the chemical potential are transported from the cold contact to the hot contact. Although the movement of electrons (from the hot end to the cold end) and holes (from the cold end to the hot end) occurs, the net current is not zero.

Now, assuming an elastic resistor approximation for a small device assuming that heating losses $(I^2R)$ occur only at the terminals, then the total number of electrons in the channel can be expressed by Eq. (6).

$$\begin{pmatrix} \text{Total number of} \\ \text{electrons} \\ \text{in the channel} \end{pmatrix} = \begin{pmatrix} \text{Number of} \\ \text{electrons} \\ \text{travelling per second} \end{pmatrix} \times \begin{pmatrix} \text{Time spent in} \\ \text{the channel} \end{pmatrix} \tag{6}$$

Eq. (6) can be rewritten, as shown in Eq. (7).

$$\left(\frac{D \times q \times v}{2}\right) = \left(\frac{I}{e}\right) \times (t) \tag{7}$$

where $D$ is the density of state of electrons, $e$ is the charge of electrons, $v$ is the electron drift velocity along the current direction, $I$ is an electric current, and $t$ is the time spent by electrons in the channel [32].

From Eq. (7), the conductance $(G)$ can be expressed as shown in Eq. (8).

$$\frac{\text{current}}{\text{voltage}} = G = \int_{-\infty}^{+\infty} dE\left(\frac{\partial f_0}{\partial E}\right) G(E) \tag{8}$$

where $G(E)$ is the conductance function whose average occurs at an energy range of $\sim 2k_B T$ around the electrochemical potential and is expressed as [32]

$$G(E) = \frac{e^2}{2t(E)} D(E) \tag{9}$$

Then, the ballistic conductance $(G_B)$ can be expressed as:

$$G_B(E) = \int_{-\infty}^{\infty} dE \frac{e^2 D(E) v(E)}{2L}[f_h(T_h, \mu_h) - f_c(T_c, \mu_c)] \tag{10}$$

where $e$ is the electric charge, $D(E)$ is the density of state, $v(E)$ is the electron drift along the direction of the current, $L$ is the length of the device, and $f_h(T_h, \mu_h) - f_c(T_c, \mu_c)$ is the difference in the Fermi function near the electrochemical potential [32].

Expanding Eq. (10) by assuming small-applied voltages,

$$f_h(T_h, \mu_h) - f_c(T_c, \mu_c) = \left(-\frac{\partial f}{\partial \mu}\right)(\mu_h - \mu_c) \tag{11}$$

where

$$\left(-\frac{\partial f}{\partial \mu}\right) = \left(-\frac{\partial f}{\partial E}\right)(\mu_h - \mu_c) = \left(-\frac{\partial f}{\partial E}\right)eV \tag{12}$$

Similarly, the average velocity ($V$) of the charges multiplied by the density of the state is directly proportional to the number of channels (modes)

$$M(E) = \frac{hD(E)V(E)}{4L} \tag{13}$$

where $h$ is the Planck's constant.

Using Eqs. (12) and (13), Eq. (10) can be further expressed as:

$$G_B(E) = \int_{-\infty}^{+\infty} dE e^2 \frac{M(E)}{h}\left(-\frac{\partial f}{\partial E}\right) \tag{14}$$

where $M(E)$ is the number of propagating modes in the channel.

Similarly, for non-ballistic conduction, i.e., diffusive conduction, $G_D$, where the length of the device is far greater than the mean free path, ($L \ggg mfp$), the conductance becomes:

$$G_D(E) = \int_{-\infty}^{+\infty} \frac{e^2}{h} M(E)\left(-\frac{\partial f}{\partial E}\right)\frac{mfp}{L+mfp} \tag{15}$$

where $mfp$ is the mean free path of electrons. Here, the expression $\frac{mfp}{L+mfp} = T(E)$, where $T(E)$ is the transmission.

Now, considering a temperature-driven current ($I_c$), which is due to the thermoelectric effect, the general expression for $I_c$, according to the Landauer-Boltzmann relation that considers the effect of temperature, is

$$I_c = \frac{1}{e}\int_{-\infty}^{+\infty} dE G(E)\left(-\frac{\partial f}{\partial E}\right) \tag{16}$$

$$I_c = \frac{1}{e}\int_{-\infty}^{+\infty} dE G(E)(f_h(E,\mu_h,T_h) - f_c(E,\mu_c,T_c)) \tag{17}$$

This can be expanded to the form of

$$\begin{aligned} I_c &= \frac{1}{e}\int_{-\infty}^{+\infty} G(E)(f_h(E,\mu_h,T_h) - f_c(E,\mu_c,T_c)) \\ &= G\left(\frac{\mu_h - \mu_c}{e}\right) + G_S(T_h - T_c) \end{aligned} \tag{18}$$

Or,

$$I_c = G\Delta V + G_S\Delta T \tag{19}$$

here, $G$ is the voltage-driven current contribution to the Seebeck coefficient, and $G_S$ is the temperature-driven current contribution to the Seebeck coefficient such that

$$G_S = \int_{-\infty}^{+\infty} dE\left(-\frac{\partial f}{\partial E}\right)G(E)\frac{E-\mu}{eT} \tag{20}$$

Eq. (19) is rearranged as:

$$\Delta V = \frac{1}{G}I - \frac{G_S}{G}\Delta T \tag{21}$$

For the experimental perspective, the first term on the right turns to zero ($I = 0$) where $\frac{1}{G}$ is a constant for open circuit measurement. In this case, the Seebeck coefficient becomes $\left(-\frac{G_S}{G}\right)$, which is mainly symbolised as "$S$" or "$\alpha$" and therefore found to be $\frac{E-\mu}{eT}$.

From Eq. (20), it is mathematically explained that $G_S$ is negative for all conductions with energy less than the electrochemical potential and positive when energy is greater than the electrochemical potential. This respectively makes the Seebeck coefficient "–" or "+" for an n-type and p-type semiconductor.

In the Peltier effect shown in Fig. 1(e), the current is made to pass through the thermoelectric device. The applied potential difference leads to a temperature gradient at the two contacts. The application of the positive potential to contact 2, as shown in Fig. 1(e), causes a drop in the chemical potential, i.e., $\mu_h > \mu_c$ and this leads to electrons flowing from contact 1 to contact 2. On the other hand, electrons from contact 1 absorb the energy of $Q_{absorb} = \mu_h - E$. For these electrons to reach contact 2, it loses the energy $Q_{lost} = E - \mu_c$. This process leaves contact 1 to cool down while contact 2 heats up. This process continues until an equilibrium is reached where no electron is transported to either side and $T_h < T_c$. This is the cooling effect described by Peltier. Within the framework of the thermoelectric material as an elastic resistor, $Q_{absorb} - Q_{lost} > \mu_c - \mu_h$. This implies that the applied power is greater than the generated power. Therefore, the thermoelectric material is an inelastic resistor and therefore dissipates heat within the individual legs. However, for ease in understanding and simplicity in the model, the inelastic TE material can be understood as several elastic resistors put in series. This will, therefore, compose of elastic portions and heat exchanging contacts within the TE material. In such a case, the heat current ($I_h$) is also generated from Eq. (13) as:

$$I_h = \frac{1}{e^2}\int_{-\infty}^{+\infty} dE G(E)[f_1(E,\mu_1,T_1) - f_2(E,\mu_2,T_2)](E-\mu) \tag{22}$$

Also, after linearization of the general form of the heat current,

$$I_h = \pi I + (\text{Constant})\Delta T \tag{23}$$

where $I$ is the regular current, and $\pi$ is the Peltier coefficient. The Peltier coefficient is related to the Seebeck coefficient as $\pi = TS$, which is $\frac{E-\mu}{e}$ by comparing Eqs. (17) and (22).

## 2.2 Derivation of the thermoelectric transport properties

For determining the electrical conductivity, Seebeck coefficient, carrier concentration, and electronic thermal conductivity of a thermoelectric material, more conveniently, the steady-state solution to the Boltzmann transport equation [24, 25] is used. This is related to Eq. (24) [20, 26], viz

$$f - f_0 = -v\tau\frac{\partial f_0}{\partial E}\left(\frac{E-\mu}{T}\nabla_x T + e\varepsilon\right) \tag{24}$$

where $v$ is the velocity vector, $\tau$ is the relaxation time of electrons, $f_0$ is the electron distribution at equilibrium, $e$ is the electrical charge, $\varepsilon$ is the electric field intensity, $\mu$ is the electrochemical potential, $E$ is the electron energy, and $T$ is the temperature.

### 2.2.1 Hall carrier concentration, mobility and the effective mass of TE materials

To ensure a higher Seebeck coefficient, there must be a single type of conduction carrier. Thus, the presence of different charge carriers (n-type and p-type) results in the cancellation

of the induced Seebeck voltage. This is because both carriers get transported to the cold end of the materials when the material is subjected to a temperature gradient. The carrier concentration ($n$) can be extracted from:

$$n(E) = \int_0^\infty dE g(E) f_0(E) \qquad (25)$$

where $g(E)$ is the density of state (DOS), which describes the states available for electrons at energy level $E$ [31], and $f_0(E)$ is the Fermi function defining the distribution of free charge carriers.

Similarly, the drift mobility for free charge carriers is given by

$$\mu_{drift} = \frac{1}{\rho n e} \qquad (26)$$

where $n$ is the carrier concentration, $e$ is the electronic charge, and $\rho$ is the electrical resistivity.

### 2.2.2 Electrical conductivity

In thermoelectricity, consideration is given to the flow of charge current as well as the heat current. The charge current flow ($J_{cc}$) is the transportation of free charge carriers from the hot to the cold end or vice versa, whereas the heat current ($\Lambda_{hc}$) is the heat conduction by the charge carriers. These two transport properties are expressed mathematically as:

$$J_{cc} \equiv nev \qquad (27)$$

Using Eq. (26), Eq. (27) could be modified as

$$J_{cc} \equiv nev = e \int_{-\infty}^{+\infty} dE g(E)[f(E) - f_0(E)]v(E) \qquad (28)$$

where $v(E)$ is the velocity of carriers, and $e$ is the electron charge.

Similarly, the $\Lambda_{hc}$ is expressed as [36]

$$\begin{aligned}\Lambda_{hc} &\equiv nV(E - \mu) \\ &= \int_{-\infty}^{+\infty} dE g(E)[f(E) - f_0(E)]v(E)(E - \mu)\end{aligned} \qquad (29)$$

From this, the electrical conductivity without temperature gradient using Ohm's law is deduced as

$$\sigma = \frac{J}{\varepsilon}\Big|_{\nabla_x T = 0} \qquad (30)$$

where $\varepsilon$ denotes the electric field intensity [37].

So, using Eq. (28) and Eq. (30)

$$\sigma \equiv \frac{J}{\varepsilon}\Big|_{\nabla_x T = 0} = \frac{e}{\varepsilon} \int_{-\infty}^{+\infty} dE g(E)[f(E) - f_0(E)]v(E) \qquad (31)$$

$$\sigma = \frac{e}{\varepsilon} \int_{-\infty}^{+\infty} dE v(E) v\tau \left( \frac{E - \mu}{T} \Delta_x T + e\varepsilon \right) g(E) \left( \frac{-\partial f_0}{\partial E} \right) \qquad (32)$$

Therefore, the electrical conductivity becomes:

$$\sigma = e^2 \int_{-\infty}^{+\infty} dE v^2(E) g(E) \tau \left( \frac{-\partial f_0}{\partial E} \right) \qquad (33)$$

### 2.2.3 Seebeck coefficient

To determine the Seebeck coefficient of thermoelectric materials, we recall the solution to the steady-state Boltzmann transport equation.

Based on the derivation of Eq. (29), the Seebeck coefficient

could be expressed by considering both the electric field and temperature contribution. Finally, the equation is solved by setting $J = 0$.

$$J = \int_{-\infty}^{+\infty} ev\tau dE g(E) \left( \frac{\partial f_0}{\partial E} \right) \left( e\varepsilon + \frac{E - \mu}{T} \nabla_x T \right) v = 0 \qquad (34)$$

From Eq. (34), expanding and rearranging, one can estimate the electric field as

$$\varepsilon = -\frac{\nabla_x T \int_{-\infty}^{+\infty} v\tau dE g(E) v(E) \left( \frac{\partial f_0}{\partial E} \right) \left( \frac{E - \mu}{T} \right)}{e \int_{-\infty}^{+\infty} ev\tau dE g(E) v(E) \left( \frac{\partial f_0}{\partial E} \right)} \qquad (35)$$

Having obtained the electric field expression and using the relation [20, 28]

$$S = \frac{\varepsilon}{\nabla_x T}\Big|_{J=0} \qquad (36)$$

The Seebeck coefficient is expressed by substituting Eq. (35) into Eq. (36)

$$S = \frac{1}{eT} \left[ \mu - \frac{\int_{-\infty}^{+\infty} dE v^2(E) \tau E g(E) \left( \frac{\partial f_0}{\partial E} \right)}{\int_{-\infty}^{+\infty} \tau dE v^2(E) g(E) \left( \frac{\partial f_0}{\partial E} \right)} \right] \qquad (37)$$

### 2.2.4 Electronic thermal conductivity

The electronic thermal conductivity is derived by expanding Eq. (29)

$$\begin{aligned}\Lambda_{hc} = &\int_{-\infty}^{+\infty} dE g(E)[f(E) - f_0(E)]v(E)E \\ &- \mu g(E)[f(E) - f_0(E)]v(E)\end{aligned} \qquad (38)$$

$$\begin{aligned}= &\int_{-\infty}^{+\infty} dE g(E)[f(E) - f_0(E)]v(E)E \\ &- \mu \int_{-\infty}^{+\infty} dE g(E)[f(E) - f_0(E)]v(E)\end{aligned} \qquad (39)$$

The second term (2$^{nd}$ term) of Eq. (39) can be expressed as;

$$\begin{aligned}\Lambda_{hc} = &\int_{-\infty}^{+\infty} dE g(E)[f(E) - f_0(E)]v(E)E \\ &- \frac{\mu}{e} e \int_{-\infty}^{+\infty} dE g(E)[f(E) - f_0(E)]v(E)\end{aligned} \qquad (40)$$

but

$$e \int_{-\infty}^{+\infty} dE g(E)[f(E) - f_0(E)]v(E) = J \qquad (41)$$

Therefore, Eq. (41) becomes

$$\Lambda_{hc} = \int_{-\infty}^{+\infty} dE g(E)[f(E) - f_0(E)]v(E)E - \frac{\mu}{e}J \qquad (42)$$

Using $\kappa_e J = 0$, Eq. (42) becomes,

$$\Lambda_{hc} = \int_{-\infty}^{+\infty} dE g(E)[f(E) - f_0(E)]v(E)E \qquad (43)$$

Similarly,

$$\kappa_e = -\frac{\Lambda_{hc}}{\nabla_x T}\Big|_{J=0} \qquad (44)$$

Using Eqs. (43) and (44) leads to

$$\kappa_e = -\frac{1}{\nabla_x J} \int_{-\infty}^{+\infty} E dE g(E)[f(E) - f_0(E)] \nu(E) \qquad (45)$$

$$= -\frac{1}{T} \int_{-\infty}^{+\infty} dE \nu^2 \tau g(E) \left(-\frac{\partial f_0}{\partial E}\right)(E - \mu) \qquad (46)$$

$$= -\frac{e\varepsilon}{\nabla_x T} \int_{-\infty}^{+\infty} dE \nu^2 \tau g(E) \left(-\frac{\partial f_0}{\partial E}\right) \qquad (47)$$

Therefore, substituting Eq. (35) into Eq. (47)

$$\kappa_e = -\frac{1}{T} \left[ \int_{-\infty}^{+\infty} dE \nu^2 \tau E^2 g(E) \left(-\frac{\partial f_0}{\partial E}\right) \right.$$
$$\left. - \frac{\left( \int_{-\infty}^{+\infty} dE \nu^2 \tau E g(E) \left(-\frac{\partial f_0}{\partial E}\right) \right)^2}{\int_{-\infty}^{+\infty} dE \nu^2 \tau g(E) \left(-\frac{\partial f_0}{\partial E}\right)} \right] \qquad (48)$$

Hence, the lattice thermal conductivity is obtained by subtracting the electronic thermal conductivity from the measured total thermal conductivity.

Equations (25), (33) and (37) represent the obtained expression for the electron density, electrical conductivity, and the Seebeck coefficient of thermoelectric materials, respectively. Based on the derived thermoelectric parameters from the Landauer-Boltzmann approach, we substantiated that electrical conductivity ($\sigma$), Seebeck coefficient ($S$) and the thermal conductivity show reliance on the charge carrier concentration ($n$). This brings about the interdependency of the electrical conductivity and the Seebeck coefficient on the electron density. In this regard, the increase in the charge carrier density leads to an increase in both electrical and thermal conductivity while reducing the Seebeck coefficient. This is not wanted when a power factor ($S^2\sigma$) enhancement is required. In this case, isovalent substitution controls the carrier density while improving carrier mobility. The improvement offered in the mobility through the isovalent substitution enhances the electrical properties without compromising the Seebeck coefficient.

## 3   The advancement of $M_2C_3$ (M = Bi, Sb and C = S, Se, Te) materials in TE application

MC thermoelectric materials have attracted immersed attention, predominately with metals from bismuth (Bi) and antimony (Sb) and chalcogenides from sulfur (S), selenium (Se) and tellurium (Te) and have been applied in room temperature thermoelectric applications [38]. Several of these materials are found to possess the same rhombohedral crystal structures with a space group of $R\bar{3}m$. Figures 2(a)–2(c) depicts the crystal structures of $Bi_2Te_3$, $Bi_2Se_3$, and $Bi_2S_3$ and Table 1 depicts the lattice parameters and the energy gap for all the discussed materials. $Bi_2Te_3$ type TE materials are known to crystallise into complex layered structures consisting of heavy atoms with a narrow energy band structure. This is responsible for the higher electrical conductivity and hence the high-power factor. The improved performance of the $Bi_2Te_3$ based materials has led to its commercialisation. Despite the great achievement in $Bi_2Te_3$ over its counterparts resulting in
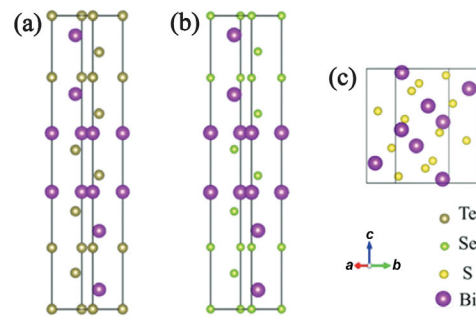


**Figure 2**   The crystal structure of (a) $Bi_2Te_3$ (b) $Bi_2Se_3$ and (c) $Bi_2S_3$. Adapted with permission from Ref. [8], © Wiley-VCH GmbH, 2016.

**Table 1**   Physical properties of $M_2C_3$ (M = Sb, Bi and C = S, Se, Te) thermoelectric materials [39–41]

|  | $Sb_2Te_3$ | $Bi_2S_3$ | $Bi_2Se_3$ | $Bi_2Te_3$ |
|---|---|---|---|---|
| Structure type | Hexagonal | Orthorhombic | Hexagonal | Hexagonal |
| $a$ (Å) | 4.26 | 1.1130 | 4.14 | 4.38 |
| $b$ (Å) | 4.26 | 1.1250 | 4.14 | 4.38 |
| $c$ (Å) | 30.45 | 0.3971 | 28.64 | 30.48 |
| Band energy (eV) | 0.22 | 1.3 | 0.3 | 0.15 |

a zT ~1, more is expected from researchers to further improve this performance.

Moreover, MC structures easily allow for dopants, which leads to the formation of either p-type or n-type semiconductors. This plays a significant role in improving the performance of the TE device. For instance, $PbTe/PbSe_{0.9}Te_{0.02}$ quantum-dot superlattice, grown by molecular beam epitaxy, showed a zT of 3.6 at 580 K [42]. Similarly, a zT of 2.6 was demonstrated in SnSe at 923 K for a single crystal [43], and sodium (Na) doped full-scale-structured of PbTe exhibited a maximum zT of 2.2 at 915 K [44].

Numerous researchers have investigated several materials and synthesis routes with an increasing desire to realise a better performing thermoelectric device [45, 46]. Crystallite size and material purity are factors dictated by the synthesis method and similarly affect the transport properties of a given material. Higher purity and smaller crystallite sizes enhance the transport properties. Several MCs have been synthesised through solvothermal/hydrothermal means [47–53], microwave-assisted synthesis [54, 55], sonochemical method [56–60], ball milling [61–63], arc melting method [64], and solid-state reactions [65–67]. Although the various synthesis methods have a unique influence on the microstructural properties and the overall performance of the underlying material, a detailed analysis of each synthesis approach on the TE performance is not captured in this review. Isovalent substitution offers a practical approach to reduce the influence of synthesis procedure while enabling the simultaneous enhancement in the Seebeck coefficient and electrical conductivity. These materials will play a significant role in the rejuvenation of TE devices in the commercial market.

### 3.1   Isovalent substitution effect in MCs and its thermoelectric properties

An isovalent substitution refers to the mechanism of substituting a host atom with an impurity atom when the impurity atom possesses the same valence number as that of the host atom. In this doping system, a neutral ion is formed and contributes

to the rearrangement of the innermost (core) energy levels situated deep in the valence band of the host atom. This idea is crucial as it is associated with the redistribution of electrons within the host atoms, consequently altering the position of the electrochemical potential and the conduction electron density.

Isovalent substitution has opened a new doping approach with numerous fundamental advantages compared with the conventional method of introducing an impurity atom to the host. In the conventional doping system, an impurity atom is deliberately introduced into the host, which leads to the formation of an acceptor or donor level in the atom, thereby increasing the charge carrier density (electrons or holes). This leaves the impurity atom ionised. The ionised atom contributes to the scattering effect of the conduction electrons and hence lowers the electron mobility [68]. The isovalent dopant possesses the same number of valence electrons as the host. The transfer of charges to the host atom leaves the impurity atom with a neutral charge. This results in the minimal scattering of conduction electrons. Furthermore, isovalent substitution creates resonant states in the host material. Hoang et al. [69] reported two defect states, i.e., deep defect (DD) state and hyper deep defect (HDD) states, in PbTe due to the isovalent doping of In, Ga, and Tl, leading to the non-rigid band approximation. The hyper deep defect states are situated ~5 eV below the valence band of the Fermi level and represent the bonding state analogous to that of molecular states. Nevertheless, increasing the impurity concentration creates a strong interaction between HDD and deep defect states. The DD state serves the purpose of resonant states and helps to maximise the Seebeck coefficient through the density of state distortion in PbTe without appreciably affecting the carrier concentration [70, 71]. The density of state (DOS) increment due to the impurity atom results in the Seebeck coefficient enhancement independent of temperature [72].

In the theoretical work of Heremans et al. [73], they demonstrated a similar effect as indium (In) was doped in place of bismuth, which is mostly trivalent). Figures 3(a)–3(d) represent the evolution of the density of states for the In substitution. Their *ab initio* electronic structure calculations revealed the HDD states, which are present below the valence band (far from the Fermi level) and seemingly, forms localised states. This state strongly influences the electronic transport properties of the system. Figures 3(e)–3(h) reveal the vital feature of the resonant-like sharp peak found in the DOS at approximately −5 eV situated just below the valence band [73].

Walukiewicz et al. [74] presented experimental work on the anti-crossing interaction, which persists between the localised states of the isovalent impurity and the extended state of the semiconductor matrix for both $ZnTe_{1-x}S_x$ and $ZnTe_{1-x}Se_x$. This predicts the electronic properties of the alloy. The mechanism of introducing a highly electronegative atom from the chalcogenides group into a metallic compound is to create a low-lying level located close to the conduction band edges. This promotes the interaction of both the localised and the extended levels leading to improvement in the electronic characteristic of the alloy. To summarize, the system of isovalent substitution is an effective doping technique to enhance the thermoelectric material performance through the formation of defects states, which serve as resonant levels via the density of state distortion. More so, unlike the conventional doping system, isovalent doping reveals a departure from the rigid band approximation, which is salient in improving the electron
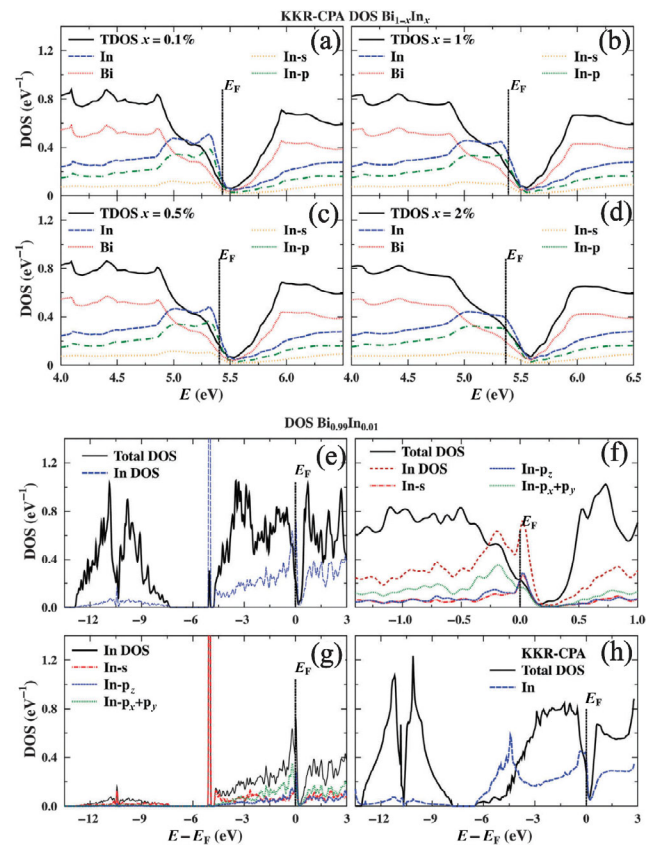


**Figure 3** The DOS evolution for $Bi_{1-x}In_x$ obtained from the KKR-CPA calculation. The Bi and In individual atomic contributions are related. (a) $x = 0.1\%$ (b) $x = 0.5\%$ (c) $x = 1\%$ (d) $x = 2\%$. (e)–(g) DOS from FP-LAPW supercell calculated result obtained for $Bi_{0.99}In_{0.01}$. (h) KKR-CPA result. The overall DOS in (a)–(c) is averaged over the number of atoms in the supercell (96) for easy comparison with the DOS (h) The DOS of the impurity atom. Adapted with permission from Ref. [73], © The Royal Society of Chemistry 2015.

density of the state and eventually enhances the Seebeck coefficient. The Seebeck coeffient is a function of the density of state (Eq. (37)) and therefore increase in the density of state effective mass, increases the Seebeck coefficient.

## 3.2 A recent development on the isovalent substitution effect in MCs TE performance

Over the past few decades, several techniques for enhancing TE materials have emerged. Some techniques that aim to enhance the power factor are resonant state doping [71], band convergence [75], quantum confinement [76], minority carrier blocking [77], while others focus on reducing the total thermal conductivity using nanostructuring [78–80], hierarchical architecture [81–83]. Researchers have employed the above techniques to improve the TE properties of all kinds of materials, including MCs [84–86], skutterudites [87–90], half Heusler [91–93], silicide [94, 95] and oxides [96–99]. Focusing on enhancing TE performance in MCs using isovalent substitution, it will be shown below how it has revolutionised the thermoelectricity sector.

In a recent work [100], the influence of isovalent substitution of Bi with cerium (Ce) for simultaneous improvement in the Seebeck coefficient, electrical conductivity and power factor in an n-type $Ce_xBi_{2-x}Se_3$ ($x = 0, 0.15, 0.3, 0.4$) thermoelectric material was studied. It was shown that the substitution of
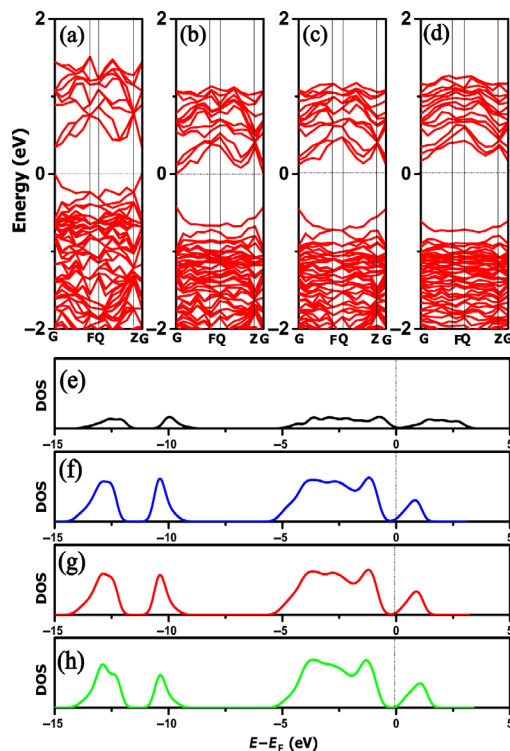
the same valent (Ce) for Bi (host) leaves the atomic structure neutral, which eradicates ionised impurity scattering and hence contribute less to conduction electron scattering near the Fermi energy. This idea was substantiated by the enhanced mobility and controlled carrier concentration with reduced doping in the experimental data. This led to an improved effective mass ($m^\star$) which is crucial for an enhanced Seebeck coefficient.
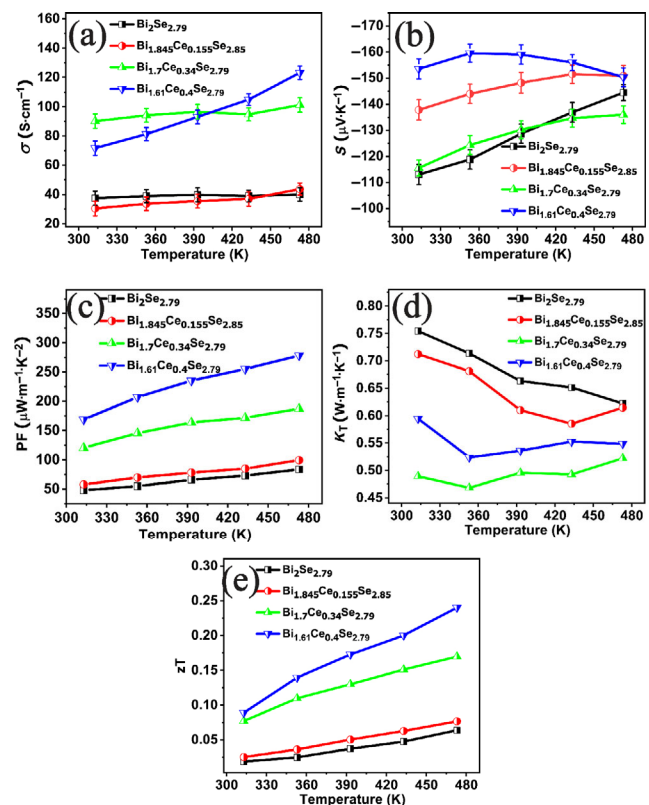
Rare earth elements form intermetallic compounds with their 4f energy levels positioned near the Fermi level and hence forms a narrow-parabolic band leading to an improved density of state at Fermi level with improved Seebeck values [4]. Therefore, it is not surprising that the $m^\star$ of the Ce-doped samples is higher than the undoped sample.

To explore the impact of the isovalent substitution of Ce for Bi atoms in $Bi_2Se_3$ topological insulator, a density functional theory (DFT) study of the density of states of isovalently doped materials was carried out (Fig. 4) [100]. It is evident from Figs. 4(e)–4(h) that the gradual shift of the Fermi level from the valence band with increasing Ce substitution is attributed to the increase in the effective mass of carriers. Similarly, the doping-induced increase in the band energy with increasing Ce concentration coupled with the hybridisation of Bi-Se orbitals for the intrinsic and doped materials near the Fermi level accounted for the enhanced $m^\star$ with Ce-doping.

DFT calculation also showed broadening and a downward shift of the valence band with Ce substitution. This was shown in all the compositions with $x < 0.4$, enabling simultaneous improvement in $S$ and $\sigma$, along with the entire temperature range (Figs. 5(a) and 5(b)), resulting in an improved power factor (Fig. 5(c)) as evident from Eqs. (33) and (37). However,
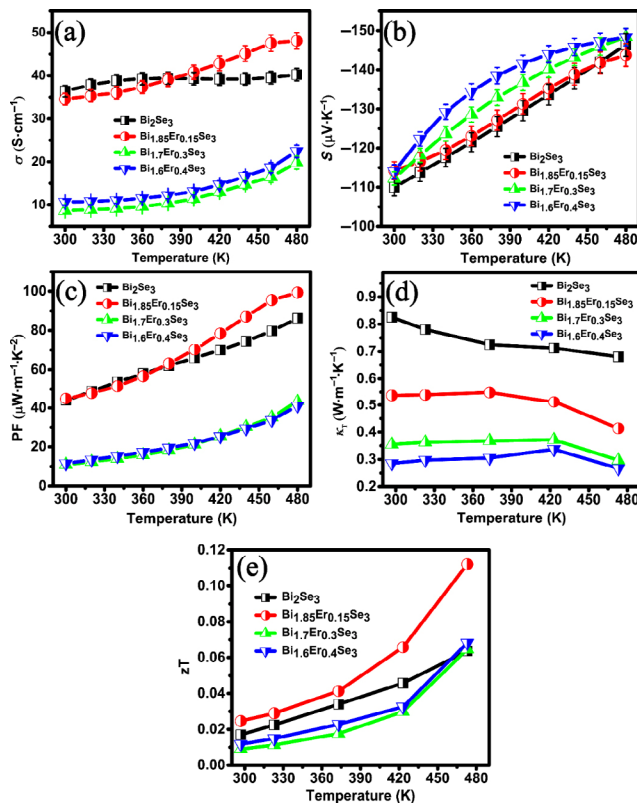
**Figure 5** Temperature dependence of the (a) electrical conductivity (b) Seebeck coefficient (c) calculated power factor (d) the total thermal conductivity (e) the thermoelectric figure of merit of the $Bi_{2-x}Ce_xSe_3$ samples. Adapted with permission from Ref. [100], © American Chemical Society 2019.

for $x = 0.4$, the intrinsic excitation occurred at 353 K, which led to a decline in the Seebeck coefficient. This was accompanied by low thermal conductivity with increasing Ce substitution (Fig. 5(d)), leading to a maximum power factor and zT of 278 $\mu W \cdot m^{-1} \cdot K^{-1}$ and 0.24, respectively at 473 K for the $Ce_{0.4}Bi_{1.6}Se_3$ sample (Fig. 5(d) and 5(e)). We proposed to use a larger atomic size rare earth metal erbium (Er) in $Bi_2Se_3$ to further elucidate the impact of size (rare earth metal) on the simultaneous enhancement of the electrical conductivity and Seebeck coefficient (Fig. 6). Although the influence of dopants with a larger atomic size is seen as causing a faster rate of deterioration of the electron mobility of the final $Bi_{2-x}Er_xSe_3$ composition, the simultaneous enhancement of the Seebeck coefficient and electrical conductivity was restored. It is also explained from the Hume Rothery (H-R) relation that atomic mismatch in a solid solution influences the lattice distortion. The mismatch is due to the larger value of the atomic factor (exceeding 15%) [101]. The calculated atomic mismatch in the $Bi_{2-x}Er_xSe_3$ was ~ 50%. This lattice distortion for the Er substitution was responsible for the massive reduction in electron mobility [102]. It is worth noting that, besides the contribution from the atomic mismatch and the scattering effect on electron mobility, chemical bond type (ionic or covalent) also significantly influences electron mobility [5]. Covalent bonds are more favourable for the transport of carriers (higher covalent bonds increase the mobility of carriers) compared to ionic bonds [103]. Thus, the ionic bond component of any A-B type bond is calculated by using the Pauli empirical formula Eq. (49).

**Figure 4** The band structures of (a) $Bi_2Se_3$, (b) $Ce_{0.15}Bi_{1.85}Se_3$, (c) $Ce_{0.3}Bi_{1.7}Se_3$ (d) $Ce_{0.4}Bi_{1.6}Se_3$ elucidating a downward shift of the valence band and the calculated total density of state (TDOS) of (e) $Bi_2Se_3$, (f) $Ce_{0.15}Bi_{1.85}Se_3$, (g) $Ce_{0.3}Bi_{1.7}Se_3$, (h) $Ce_{0.4}Bi_{1.6}Se_3$. Adapted with permission from Ref. [100], © American Chemical Society 2019.

**Figure 6** Temperature dependence of the (a) electrical conductivity, (b) Seebeck coefficient, (c) calculated power factor, (d) the total thermal conductivity, (e) the thermoelectric figure of merit of the $Bi_{2-x}Er_xSe_3$ samples. Adapted with permission from Ref. [102], © Published by Elsevier B.V. 2020.

higher than that of doped Er-Se ($Bi_{2-x}Er_xSe_3$) samples. It is evident that a lower degree of covalent bonding in the Er-Se containing samples leads to low electron mobility.

Despite the deterioration of the carrier mobility with doping, the simultaneous enhancement of the Seebeck coefficient and electrical conductivity was sustained due to an optimised carrier density which compensated for the low carrier mobility [102]. Low thermal conductivity of 0.41 W·m⁻¹·K⁻¹ was obtained for $Bi_{1.85}$ $Er_{0.15}Se_3$ at 473 K.

An experimental study of sulfur-substituted $Bi_{0.49}Cu_{0.01}Sb_{1.5}Te_3$ materials was carried out by Lee et al. [104] to improve TE performance. The isovalent substitution of S in the $Bi_{0.49}Cu_{0.01}Sb_{1.5}Te_3$ structures simultaneously improves the weighted mobility of the valence band and the density of state effective mass via the control of phonon and carrier interactions. This activates the transport of holes in the $Bi_{0.49}Cu_{0.01}Sb_{1.5}Te_3$ material. Consequently, the power factor is enhanced with S-doping within the entire temperature range. Similarly, the total thermal conductivity is substantially suppressed at higher temperatures due to the activation of the p-type conduction mechanism. It is important to mention that the S doping was optimised for a doping concentration of less than 1 at.%. Therefore, the synergetic effect of the high-power factor and low thermal conductivity resulted in a high thermoelectric figure of merit (zT = 1.0 for 300 K < T < 520 K), as shown in Eq. (3).

Vaney et al. [105] investigated tellurium substitution with Se on the electronic band structure and the TE properties of $As_2Te_{3-x}Se_x$. They found that the lower substitution amount did not significantly alter the density of state and the energy gap at the Fermi level. As Se substitution increased, there was an increase in electrical conductivity and Seebeck coefficient coupled with reduced thermal conductivity. Similarly, Devender et al. [106] reported an unusual increase in electrical conductivity with an increasing Seebeck coefficient by S doping in the $Bi_2Te_2Se$ topological insulator. The results are presented in Fig. 7. In the pristine $Bi_2Te_2Se$, a Seebeck coefficient of S < −30 µV·K⁻¹ was found. However, at maximum S concentration of 2 at.% doping revealed an enhanced Seebeck coefficient to −130 µV·K⁻¹, accompanied by the highest electrical conductivity

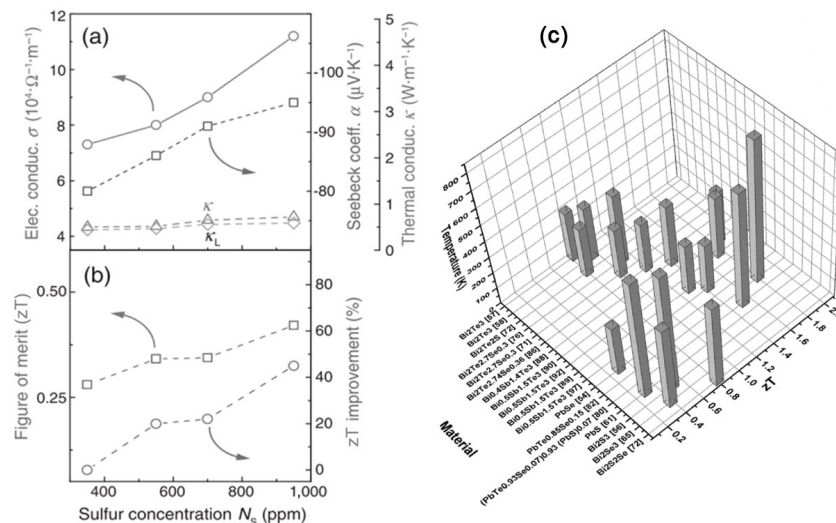$$\text{ionic bond} = 1 - \text{Exp}\left[\frac{-(X_A - X_B)^2}{4}\right] \quad (49)$$

Here, $X_A$ and $X_B$ are the electronegativities of A and B, respectively. Therefore, using the electronegativities of Er (1.24) and Bi (2.02), the estimated ionic bond component of the Bi-Se (6.85%) is found to be lower than that for the Er-Se (34.9%), so the electron mobility of pure Bi-Se appeared to be



**Figure 7** A room temperature (a) electrical conductivity (circles), Seebeck coefficient (square) and thermal properties ($\kappa_l \cdot \kappa_e$) of a nanostructured $Bi_2Te_2Se$ thermoelectric pellet, and (b) represents zT and zT improvement dependent on S concentration, $N_S$. Adapted with permission from Ref. [106], © WILEY-VCH Verlag GmbH & Co. KGaA, Weinheim 2016. (c) Comparison of the TE performance of pristine MC and isovalently doped MC material.

at 1,200 S·cm⁻¹. This could only be explained by the extreme sensitivity of the inverted band structure in $Bi_2Te_2Se$, leading to a small spin-orbit coupling [107] caused by S doping. The doping of lighter chalcogenides (S) compared to Se and Te reduces the spin-orbit coupling [108–110]. In the work of Devender et al., electron mobility decreased with increasing temperature and S doping concentration. This observation is because of extrinsic scattering by local and extended defects in the metal–like conduction behaviour of the $Bi_2Te_2Se$ [7].

In our recent studies [111], a modified Wang et al. synthesis method [111] is adopted to investigate indium (In) and antimony's (Sb) dual isovalent substitution effect on bismuth telluride thermoelectric materials. Figures 8(a)–8(f) represents the measured TE properties compared with pristine $Bi_2Te_3$. It was evident from the DFT calculation that the dual doping of In and Sb introduces defect states near the Fermi level, which influences the electronic and thermal properties of the system via density of state optimization and phonon-induced scattering, respectively. A noticeable degradation of the carrier mobility accompanied by mild improvement in carrier density was observed, attributed to the structural complexity-induced lattice distortion, which offers opposition to both phonon and electron transport. The consequence of this is improved electron and phonon scattering, leading to ultralow total thermal conductivity (Fig. 8(d)). A maximum zT of 0.54 at 423 K (Fig. 8(e)) was obtained for 0.1 at.% doping ($x = 0.1$) (Fig. 8(f)), which is evident that the improved total thermal conductivity reduction compensated for the low electronic properties improves the overall TE performance. This study proved the tenability of the thermoelectric performance of $Bi_2Te_3$ based
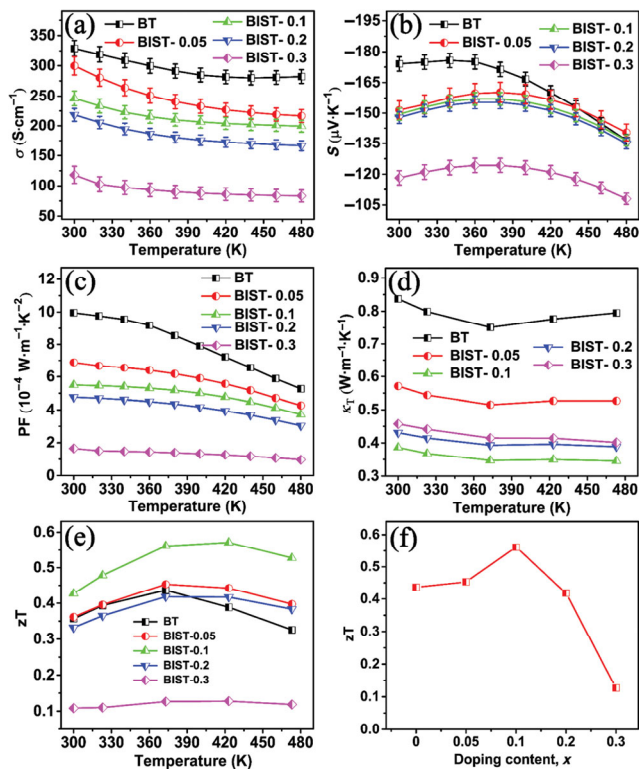


**Figure 8** Temperature dependence of the (a) electrical conductivity, (b) Seebeck coefficient, (c) calculated power factor, (d) the total thermal, (e) the TE figure of merit dependence on temperature, (f) the maximum zT dependence on doping content at 423 K for all the BIST samples (where BT = $Bi_2Te_3$, and BIST = $Bi_{2-x}In_xSb_{2x/3}Te_3$ ; $x$ = 0.05, 0.1, 0.2 and 0.3). Adapted with permission from Ref. [111], © Wiley-VCH GmbH 2021.

thermoelectric material through isovalent substitution of In and Sb.

In 2017, Liu et al. [112] utilized a modified solution method [106] in the synthesis of $Bi_2Te_{3-x}Se_x$ ($x$ = 0, 0.3, 0.43, 0.75 and 1.5) nanowire with tunable chemical compositions. Their work revealed that isovalent substitution of Te by Se (a comparatively smaller element) lowers the electrical conductivity while simultaneously improving the Seebeck coefficient and power factor. The best performing composition was $Bi_2Te_{2.7}Se_{0.3}$ with room temperature carrier density and mobility of $4.37 \times 10^{19}$ cm⁻³ and 60.22 cm²·V⁻¹·S⁻¹, respectively. This is because when the dopant (Se) with $x < 1.5$-mole percent was added, the overall carrier density decreased from $10^{20}$ cm⁻³ in pristine to $10^{19}$ cm⁻³ in $Bi_2Te_{3-x}Se_x$. Accordingly, the resulting thermal conductivity was lowered due to increased phonon scattering via the involvement of boundary induced scattering and dopant site scattering effect. These enhanced properties were essential for reaching the highest power factor of 1.27 mW·m⁻¹·K⁻¹ at 300 K. This study proved the tenability of the thermoelectric performance of $Bi_2Te_3$ based thermoelectric material through isovalent substitution of Se at the Te site, as was also reported by Soni et al. [113].

By and large, vacancies and ionised anti-sites exist in $Bi_2Te_3$ as donors and acceptors, respectively. However, it is crucial to understand that the formation of anti-site defects is more favourable than that of vacancies due to their respective formation energies ~ 0.4 and ~ 1 eV, respectively [61, 114, 115]. For an n-type $Bi_2Te_3$ semiconductor, every Te vacancy ($V_{Te}$) produces a pair of electrons whereby an anti-site defect $Te_{Bi}$ is formed through the reaction, $Te_{Te} + V'''_{Bi} + 3h^* \rightarrow Te^*_{Bi} + V^{**}_{Te} + 3e'$ in a Te-rich environment. Table 2 shows the covalent radius, the electronegativity, and the evaporation energy of Bi, Sb, Te, and Se. This illustrates that an increase in anionic vacancies with decreased antisite defects arises from an increase in Se content in $Bi_2Te_{3-x}Se_x$; however, increasing Bi content in $Bi_xSb_{2-x}Te_3$ could lead to suppression of antisite defects with no noticeable effect on the anionic vacancies [35].

That notwithstanding, through isovalent doping with Se in the $Bi_2Te_3$ system, the Se atoms substitute the $Te^2$ atoms followed by $Te^1$ atoms [117, 118], where the superscripts denote two different forms of bonding for the Te atom. This leads to a decrease in electrical conductivity due to reduced carrier density. This is so because the occupation of $V_{Te}$ by Se atoms compensates for the free electrons [119] and therefore results in increased carrier mobility, attributed to reduced carrier density [120]. More so, a higher Se doping ($x \geq 1$) in the case of Liu et al. [121], lead to reduced electrical conductivity because of the deterioration of the carrier mobility (Eq. (6)) caused by electron-phonon scattering. This is also because the substitution of Se atoms at the Bi site in $Bi_2Te_{3-x}Se_x$ improves the total carrier density without compromising the electron mobility reduction. It was observed that Se doping leads to a decrease in the total thermal properties due to increased defect density. However, along the same path, Gharsalla et al. [64]

**Table 2** Covalent radius, Electronegativity and evaporation energy for Bi, Sb, Se, and Te [116]

|  | Bi | Sb | Te | Se |
|---|---|---|---|---|
| Covalent radius | 208.98 | 121.75 | 127.6 | 78.96 |
| Electronegativity | 2.02 | 2.05 | 2.1 | 2.55 |
| Evaporation energy (KJ·mol⁻¹) | 104.8 | 77.14 | 52.55 | 37.70 |

reported the formation of donor states in the bandgap due to the partial substitution of Te by Se. This new state alters the electrical conductivity as well as the Seebeck coefficient. The Seebeck coefficient was found to increase to $-140$ $\mu V \cdot K^{-1}$ at 400 K upon Se doping, while the thermal conductivity was below 0.8 $W \cdot m^{-1} \cdot K^{-1}$ at room temperature.

Srinivasan et al. [122] in 2010, Yan et al. [123] in 2010, Kim et al. [124] in 2011, Carlton et al. [125] in 2012 and Hu et al. [126] in 2014 all reported enhancing the thermoelectric properties due to Se substitution in *n*-type $Bi_2Te_{2.7}Se_{0.3}$. Keawparak et al. [127], in 2011, prepared the same alloy ($Bi_2Te_{3-x}Se_x$) by the Bridgman method and obtained a p-type conduction type for all the Se concentrations. The Seebeck coefficient was almost independent of the Se amount, while the electrical conductivity decreased with Se impurity content. However, the total thermal conductivity decreased with Se substitution due to reduced electronic and lattice conductivities. The materials with the highest performance was found for $x = 0.36$ ($Bi_2Te_{2.64}Se_{0.36}$) at room temperature, where $\sigma = 5{,}500$ $S \cdot cm^{-1}$, $S = 220$ $\mu V \cdot K^{-1}$, $\kappa = 0.7$ $W \cdot m^{-1} \cdot K^{-1}$ and zT = 1.2. Through the microwave synthesis method, Nozariasbmarz et al. [128] reported enhanced TE properties of $Bi_2Te_{2.7}Se_{0.3}$ and glass nanocomposite materials. Seebeck coefficient of $-297$ $\mu V \cdot K^{-1}$ and ultralow thermal conductivity of 0.6 $W \cdot m^{-1} \cdot K^{-1}$ was obtained at 300 K. A peak zT of 0.87 was obtained for the optimized material. This proves to be a reliable approach to enhancing the TE properties of different materials.

Elsewhere, Lu et al. [129] reported the role of isovalent substitution for thermoelectric properties enhancement. Their work focused on the substitution of Se for S in $Cu_{12}Sb_4S_{13-x}Se_x$. It showed a drastic increase in electrical conductivity with an almost constant Seebeck coefficient for several concentrations of Se substitution. Unlike traditional doping [130–133], where the electrical conductivity enhancement is brought forth by an increase in (positive or negative) charge carrier concentration due to increased Fermi energy of electrons, the improvement offered by the isovalent substitution of Se for S resulted from an upward displacement of the valence band constituting low effective mass. Therefore, an unchanged Seebeck coefficient (Fig. 9) is achieved due to the similar density of state effective mass of the displaced valence band compared to the already existing conduction band.

This work is an essential support for demonstrating decoupling the interdependency of electrical conductivity and the Seebeck coefficient [6, 134]. The limitation on the simultaneous improvement in the electrical conductivity and the Seebeck is given by the Pisarenko relation [135–138], which is a function of carrier concentration. A power factor of 4.6 $\mu W \cdot cm^{-1} \cdot K^{-1}$ was achieved for $x = 1$ substitution compared to 2.96 $\mu W \cdot cm^{-1} \cdot K^{-1}$ for the undoped case calculated at room temperature. This represents approximately 60% enhancement on the power factor. An isovalent substitution stabilises or improves the Seebeck coefficient [129, 132] while increasing the electrical conductivity through enhancement of carrier mobility rather than the contribution from carrier concentration (Eq. (27)) [129].

Similarly, Heinrich et al. [139], in 2014, focused on the effect of the isovalent substitution of S for Se on the thermal transport properties. The room temperature thermal conductivity of $Cu_2ZnGeSe_{4-x}S_x$ showed a 42% reduction of lattice thermal conductivity, which increased zT. This effect is also supported by Chmielowski et al. [140] for Se substituting S in $CoSbS_{1-x}Se_x$, which shows a 50% reduction in thermal conductivity.

Tables 3 and 4 represent the undoped and isovalent substituted MC TE materials, respectively. The latter showed an improved TE property compared to the former. A graphical data for the two sets of materials (pristine MC and MC with isovalent doping) are depicted in Fig. 9(c).
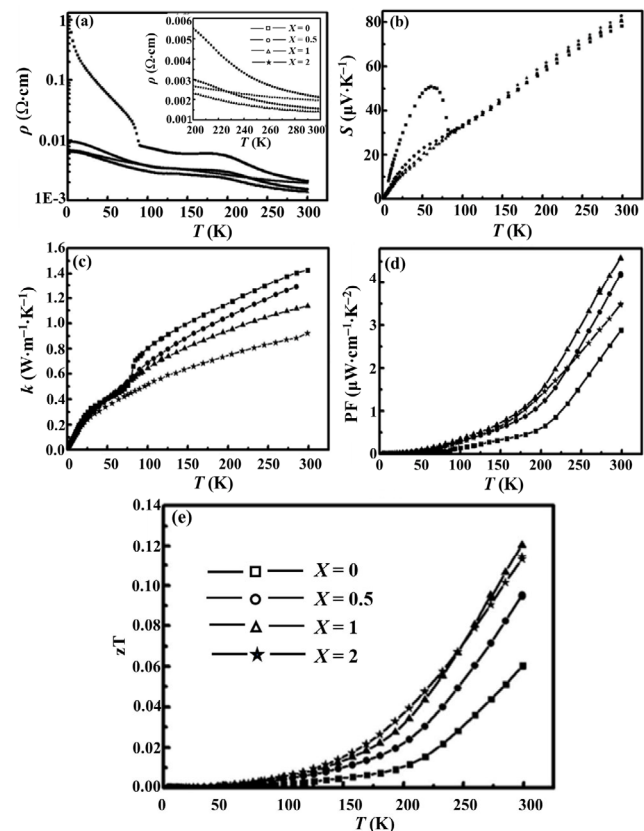


**Figure 9** Temperature dependence (a) electrical resistivity, (b) Seebeck coefficients, (c) thermoelectric power factor, (d) thermal conductivity and (e) zT of $Cu_{12}Sb_4S_{13-x}Se_x$ thermoelectric solid solution for ($x = 0$, 0.5, 1 and 2). Adapted with permission from Refs. [129], © The Royal Society of Chemistry 2016.

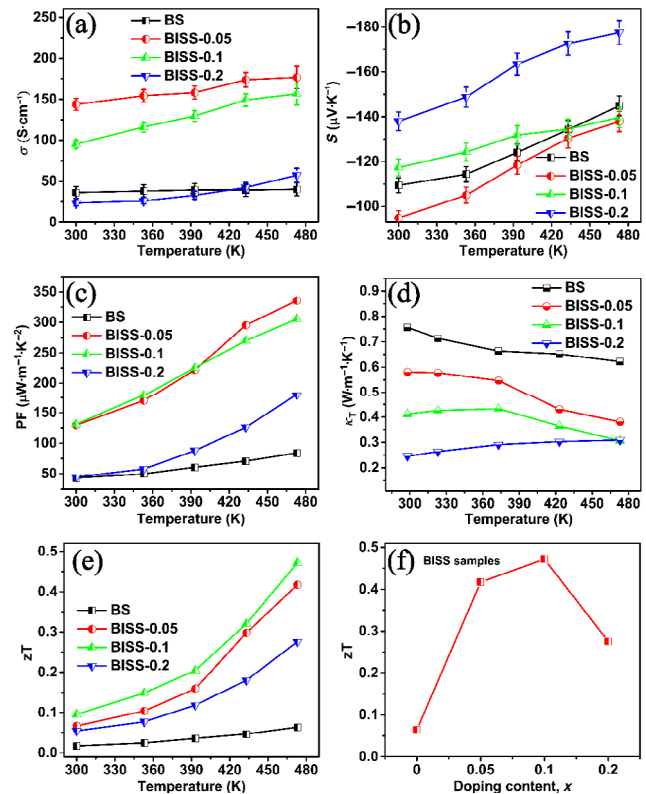**Table 3** Undoped MCs thermoelectric materials with their respective figure of merit (zT)

| TE materials | zT | Temperature, $T$ (K) | Power factor, PF ($mW \cdot mK^{-2}$) | References |
|---|---|---|---|---|
| PbSe | 0.3 | 300 | 1.3 | [141] |
| PbSe | 0.49 | 500 | 1.4 | [142] |
| $Bi_2S_3$ | 0.5 | 723 | 0.45 | [143] |
| $Bi_2Te_3$ | 0.83 | 300 | 2.1 | [144] |
| $Bi_2Te_3$ | 0.95 | 325 | 3.3 | [145] |
| $Bi_2Te_3$ | 0.4 | 300 | 2 | [146] |
| SnTe | 0.8 | 850 | 2 | [147] |
| PbS | 0.3 | 725 | 0.5 | [148] |
| $Cu_2Se$ | 0.5 | 373 | 0.9 | [149] |
| $Cu_{1.89}S$ | 0.11 | 350 | 0.4 | [150] |
| $Bi_2Se_3$ | 0.41 | 525 | 0.6 | [151] |
| $Bi_2Se_3$ | 0.38 | 550 | 0.6 | [152] |
| SnSe | 0.5 | 650 | 0.4 | [43] |
| SnS | 0.16 | 823 | 0.15 | [153] |
| $In_4Se_3$ | 0.59 | 700 | 0.4 | [154] |
| $TiS_2$ | 0.2 | 300 | 0.45 | [155] |

**Table 4** Improvement in MC TE materials obtained through isovalent substitution

| TE materials | Material type | Temperature, $T$ (K) | Figure of merit, zT | References |
|---|---|---|---|---|
| $Bi_2Te_{2.7}Se_{0.3}$ | n-type | 300 | 0.54 | [113] |
| $Bi_2Te_{2.7}Se_{0.3}$ | n-type | 300 | 1.0 | [125] |
| $Bi_2Te_{2.7}Se_{0.3}$ | n- type | 398 | 0.8 | [156] |
| $Bi2Te_{2.7}Se_{0.3}$ | n-type | 300 | 0.93 | [122] |
| $Bi_2Te_{2.7}Se_{0.3}$ | n-type | 398 | 1.04 | [123] |
| $Bi_2Te_ySe_{3-y}$ | n-type | 373 | 0.7 | [124] |
| $Bi_2Te_{2.7}Se_{0.3}$ | n-type | 425 | 1.11 | [157] |
| $AgPb_{18}SbTe_{18}Se_2$ | n-type | 523 | 0.82 | [158] |
| $Pb_{9.6}Sb_{0.2}Te_3Se_7$ | n-type | 650 | 1.2 | [159] |
| $Bi_2Te_{2.7}Se_{0.3}$ | n-type | 480 | 1.2 | [160] |
| $(PbTe_{0.93}Se_{0.07})_{0.93}$ $(PbS)_{0.07}$ | n-type | 700 | 1.52 | [161] |
| $SnTe_{1-x}Se_x$ | n-type | 860 | 0.8 | [162] |
| $PbTe_{0.85}Se_{0.15}$ | p-type | 850 | 1.8 | [75] |
| $Bi_2Te_{2.3}Se_{0.7}$ | n-type | 445 | 1.2 | [126] |
| $Bi_2Te_{2.79}Se_{0.21}$ | n-type | 300 | 1.14 | [163] |
| $Bi_2Te_2Se_1$ | n-type | 513 | 1.0 | [164] |
| $Bi_2Te_{2.74}Se_{0.36}$ | p-type | 300 | 1.2 | [127] |
| $Bi_2Te_2S$ | n-type | 300 | 0.8 | [156] |
| $Bi_2SeS_2$ | n-type | 500 | 0.8 | [156] |
| $Bi_2Te_{2.3}Se_{0.3}S_{0.4}$ | n-type | 473 | 0.7 | [156] |
| $Bi_{0.4}Sb_{1.4}Te_3$ | p-type | 300 | 0.98 | [165] |
| $Bi_{0.4}Sb_{1.4}Te_3$ | p-type | 373 | 1.4 | [166] |
| $Bi_{0.5}Sb_{1.5}Te_3$ | P-type | 300 | 1.3 | [167] |
| $Bi_{0.5}Sb_{1.5}Te_3$ | p-type | 320 | 1.86 | [168] |
| $Bi_{0.52}Sb_{1.48}Te_3$ | p-type | 300 | 1.52 | [84] |
| $Bi_{0.5}Sb_{1.5}Te_3$ | p-type | 373 | 1.75 | [169] |
| $Bi_{0.5}Sb_{1.5}Te_3$ | p-type | 323 | 1.71 | [170] |
| $Bi_{0.5}Sb_{1.5}Te_3$ | p-type | 323 | 1.56 | [171] |
| $Bi_{0.48}Sb_{1.52}Te_3$ | p-type | 350 | 1.1 | [172] |
| $Ce_{0.1}Bi_{1.9}Te_3$ | p-type | 386 | 1.22 | [173] |
| $Bi_{0.5}Sb_{1.5}Te_3$ | p-type | 300 | 1.42 | [174] |
| $Bi_{0.4}Sb_{1.6}Te_3$ | p-type | 400 | 1.36 | [175] |



**Figure 10** Temperature dependence of the (a) electrical conductivity, (b) Seebeck coefficient, (c) calculated power factor, (d) the total thermal, (e) the TE figure of merit dependence on temperature, (f) the maximum zT dependence on doping content at 473 K for all the BISS samples (where BS = $Bi_2Se_3$ and BISS = $Bi_{2-x}In_xSb_{2x}Se_3$; $x = 0.05$, 0.1, and 0.2). Adapted with permission from Ref. [176], © American Chemical Society 2022.

Our most recent article has investigated the isovalent co-doping of In and Sb in $Bi_2Se_3$ TE materials via experimental and DFT studies [176]. The experimental results show that simultaneous enhancement of the electrical conductivity and Seebeck coefficient is possible for In and Sb co-doping leading to a boost in the PF, as shown in Fig. 10. Similarly, the lattice distortion induced by this doping approach paired with the small crystallite size caused by the ionic radii difference of the host and the dopants improves the pining of the lattice vibration, thus reducing the total thermal conductivity. The measurable deterioration in the thermal conductivity instigated by the In and Sb doping coupled with the improvement in the power factor is essential for TE performance. Thus, an optimum TE performance ($zT_{max} = 0.47$ at 473 K) was obtained for a doping concentration of 0.1 at.% representing one of the best performances for $Bi_2Se_3$ materials for TE application. The DFT calculation also discovers an underlying deep defect state located at ~15 eV below the Fermi level, and Fermi energy shifts towards the conduction band minimum.

This leads to enhanced electronic properties via density of states optimization induced by the co-doping. It is worth mentioning that Bi ($6p^3$) substitution with In ($5s^25p^1$) is anticipated to restrict the scattering of conduction electrons. However, the drastic decrease in the mobility of carriers comes from the electronegativity difference between In and Bi, resulting in an increase in ionic bonding and hence increasing the DOS.

### 3.3 Other metal chalcogenides materials for TE application

#### 3.3.1 *Lead chalcogenides*

Lead chalcogenide (PbX, X = Te, Se, S) materials possess intrinsically low thermal conductivity. Therefore, by adopting a proper material design, nanostructuring, band engineering, and alloying, a boost in TE performance can be achieved. Biswas et al. reported a breakthrough in the zT of 2.2 [44] in PbX via nanostructuring. The effectiveness of the nanostructures places a suitable precipitate of nanoscale in the matrix leading to enhanced scattering of lattice vibration [177]. In search of improved TE performance in PbX, several experimental results have shown that lead chalcogenides uniquely show strong anharmonic lattice dynamics responsible for low thermal conductivity [178, 179]. Similarly, multiple valence bands ($PbTe_{1-x}Se_x$) [75] and introducing density of state distortion to the valence band (Tl–PbTe) [71] have shown excellent TE performance. Elsewhere, Chen et al. [180] has proposed a dislocation scattering model as a practical approach to reducing the lattice thermal conduction of PbX TE materials. It is

expected that this model can serve as a strategy for other thermoelectric materials to improve the figure of merit. In Chen et al. studies, cation vacancies were deliberately introduced into the solid solution of $Pb_{1-x}Sb_{2x/3}Se$, where upon thermal heat treatment, the vacancies were annihilated by creating homogenous dislocations with the grains. This result in remarkable thermal conductivity as low as 0.4 $W \cdot m^{-1} \cdot K^{-1}$ and a corresponding high zT.

Most recently, Shi et al. [181] investigated the impact of isovalent doping of selenium in $Pb_{0.98}Ga_{0.02}Te_{0.96}Se_{0.04}$ and explored the thermoelectric performance compared to the pristine. It was evident that, at low temperatures, the $Ga^+$ ions oxides to $Ga^{3+}$ upon doping with Se. This lead to an enhancement in the carrier density (Eqs. (27) and (37)) from $1.16 \times 10^{19}$ to $2.17 \times 10^{19} C \cdot m^{-3}$ constituting a power factor of 3.04 m $W \cdot m^{-1} \cdot K^{-2}$ measured at 482 K. Again, the concentration of point defects induced phonon scattering improved for the Se doped samples which contributed significantly to the lowering of the lattice thermal conductivity (0.46 $W \cdot m^{-1} \cdot K^{-1}$) and hence increased the zT of the pristine (zT = 0,74) by 112%.

### 3.3.2 Copper chalcogenides

Copper chalcogenides (CuX, X = Te, Se, S) have been given enormous attention due to their promising potential for TE applications [182, 183]. CuX composes of diamond-like chalcogenides and liquid-like binary compounds, and multinary derivatives. CuX is formed by covalent bonds, and their atomic ratios and structures vary based on the oxidation state of copper. Typically, the chalcogen atoms constitute the rigid lattice frame. In contrast, the copper atoms randomly occupy the chalcogen lattice, comprising the general features of two sublattices, promoting the decoupling of electron and phonon transport.

Similarly, the disordered and even liquid-like sublattice and complex crystal structure of CuX lead to intrinsically low thermal conductivity [182]. The presence of mixed conduction (electronic and ionic conductivity) of CuX makes them superior semiconductors. Exceptional thermoelectric performance [184, 185] is obtained from the unique electronic band structure [186], crystal structure, phase transition behaviour, and superionicity of $Cu_2Se$ materials, which contribute to a high Seebeck coefficient and low lattice thermal conductivity for a phase transition of 400 K [6, 187]. Phase transformation between monoclinic $Cu_2Se$ and superionic antifluorite $Cu_2Se$ has been shown to modify the electronic band structures and improve electrical performance [6]. The fluid-like behaviour of the Cu sublattice in an antifluorite $Cu_2Se$ and the corresponding superionicity lead to the ultralow lattice thermal conductivity and high zT at $T \sim 400$ K. Lui et al. [6] have reviewed the band structure, crystal structure, phase transition and intrinsic thermoelectric performance of $Cu_2Se$ and the potential thermoelectric properties. In his review, details have been provided on the effectiveness of improving the transport properties and the reduction of lattice thermal conductivity to boost the zT of $Cu_2Se$. It was evident that the enhancement in the zT is mainly achieved via reduction of the lattice thermal conductivity – efficient scattering of lattice vibration [188, 189]. This study is crucial as it bridges the progress gap and challenges regarding $Cu_2Se$ thermoelectrics.

Nano flakes of size ~ 200 nm have been studied by Yang et al. [190] and the thermoelectric performance is evaluated at $T = 500$–850 K. The nano-size grains form dense grain boundaries, which effectively scatters mid-wavelength phonon and hence drastically reduce the lattice thermal conductivity from 0.68 $W \cdot m^{-1} \cdot K^{-1}$ (bulk $Cu_2Se$) to 0.18 $W \cdot m^{-1} \cdot K^{-1}$ (nano-size $Cu_2Se$) leading to a zT boost from 0.7 to 1.5, respectively. The effect of nickel doping in $Cu_2Se$ has been studied by Ducka et al. [191] synthesized via reduction of reagent in hydrogen, and the influence of Ni on both microstructural and TE properties is related. The most evident structural difference was the presence of Cu precipitates in the bulk matrix for the Ni-doped samples leading to enhanced electrical conductivity (Eq. (33)) with no deterioration of the Seebeck coefficient (Eq. (37)). The observable transition of the $Cu_2Se$ phase accounted for the high zT = 0.8 obtained at 650 K.

### 3.3.3 Germanium tellurides

Group IV-VI semiconductor chalcogenides, such as GeTe, SnTe, and PbTe, have attracted emersed attention due to their remarkable TE performance in the mid-temperature (500–800 K) range [192–194]. The admirable transition from a high temperature and symmetry cubic phase (c-GeTe) to a low-temperature rhombohedral phase (r-GeTe) makes GeTe a promising TE material [195]. More importantly, the symmetry breaking in GeTe allows for diversified rearrangement of the split bands leading to a high band degeneracy. This is crucial in promoting low lattice thermal conductivity, as evidenced by the hierarchical bonds and microstructural anchor provided by the band degeneracy. The distinctive feature of energy level switching between the *L* and *S* valence bands enables an extra degree of freedom for the possibility of band manipulation, which is essential for improving the electronic properties via high band degeneracy [193, 196]. The band structure of c-GeTe is like that of PbTe and SnTe, making c-GeTe tutored a potential material for device application [197]. As such, a high zT > 2 [195, 198, 199] has been found for c-GeTe, which is superior to several of the mid-temperature p-type thermoelectric materials. The Carrier density optimization strategy was utilized by Li et al. [194] to enhance the TE performance of GeTe with Sb and Se doping. A zT of 2 was found for the Sb and Se composition, resulting in a 40% reduction in the lattice thermal conductivity compared with only Sb doping [194]. The substantial decrease in the lattice thermal conductivity with alloying indicates the efficient phonon scattering [200] instigated by the strain and mass fluctuations produced by the alloying process. Hong et al. [195] investigated the In and Sb co-doping effect of GeTe and observed an induced density of state distortion near the Fermi level. Again, the presence of the Sb and In lowers the transition temperature of the GeTe, leading to enhanced thermoelectric performance. A zT as high as 2.3 was obtained for c-GeTe thermoelectric materials. The high preformation was attributed to improved electronic transport coefficients caused by the two valence bands and the stronger phonon-phonon interaction, reducing the intrinsic lattice thermal conductivity [199]. More so, the inevitable point defect, coupled with the high density of stacking faults, grain boundaries, and nanoscale precipitate, contributed to the ultralow thermal conductivity of the synthesized GeTe TE material [194]. Elsewhere, Gelbstein et al. [198] explored the spark plasma sintering approach to study the TE performance of p-type $Ge_{0.87}Pb_{0.13}Te$ material. A significantly high TE performance (zT ~ 2) obtained for this composition could be attributed to the size twining, and nucleation of sub-micron phase separation domain existing in the synthesized composition, where the zT and the efficiency of the studies is among the highly performing GeTe materials reported so far.

### 3.3.4 Tin chalcogenides

Although lead telluride is regarded as a group IV-VI semiconductor chalcogenides material with extremely high zT, lead toxicity is problematic. Therefore, a lead-free substitute (Tin chalcogenide) with high zT is in high demand. Pristine SnSe has demonstrated a tremendous TE performance (zT ~ 2.6 at 923 K) [201] and has attracted considerable attention for high-temperature TE devices. This has uncovered and shown the great potential of non-lead-based group IV chalcogenides for TE devices due to their similar crystal structure to that of PbTe [202]. Like PbTe materials, SnSe undergoes a phase transition from a low-symmetry orthorhombic (*Pnma* space group) to a higher-symmetry orthorhombic (*Cmcm* space group) structure when the temperature approaches 750 K, responsible for the unique transport properties. This second-order transition preserves the bilayer stacking as each Sn atom is found to be coordinated by four neighbouring Se atoms or vice versa at equal distances within the *y–z* plane [203, 204]. Again, SnS possess a similar structure to that of SnSe but has low thermoelectric performance due to high electrical resistivity. By adopting a strategic doping design, the zT can be massively improved. Besides all the potentials of the single crystal SnSe as a thermoelectric material, polycrystalline SnSe is restricted in performance due to the high thermal conductivity and low electronic conductivity. Isovalent doping (Te-dopant) as an effective strategy was utilized by He et al. [205] to simultaneously enhance the electrical conductivity and reduce thermal conductivity in p-type polycrystalline SnSe. Using a two-step synthesis method, a nonequilibrium bulk $Sn(Se_{1-x}Te_x)$ solid solution with $x$ up to 0.4 at.% realized a multifold increase in the carrier density (Eq. (25)), leading to improved electrical conductivity (Eq. (33)) and reduced lattice thermal conductivity. It is worth mentioning that the larger size Te–ions in the $Sn(Se_{1-x}Te_x)$ creates a weak Sn-Te bond, resulting in the formation of a high density of Sn vacancies which leads to a reduction in the phonon frequency and improved phonon scattering. The effects of the structural changes upon the immense size of Te carrier doping beyond the equilibrium limit are enhanced thermoelectric performance in the SnSe materials.

## 4    Threats to validity

This review focused on an isovalent substitution as an optimisation mechanism for MC thermoelectric performance and did not review the application of such a technique to other thermoelectric materials such as perovskites, etc. MC consist of at least a metal and an element of group VI (called chalcogens). These materials have been regarded as the best materials in TE energy conversion due to their superior efficiencies. Therefore, they have been utilised in device fabrication for thermoelectric applications due to their high-power factor. MC have low fabrication and operational costs. Le Blanc et al. [206] reported that MCs are the most cost-effective materials for thermoelectric energy conversion, therefore attracting the most attention. Similarly, Yadav et al. [207] showed higher efficiency and stability for MC thermoelectric materials than other TE materials like oxides and tetrahedrites. As an advantage of MC, structural variations, complexity, and flexibility allow for phase transformation/transition, enabling performance enhancement. For instance, 75 wt.% of $Sb_2Te_3$ was added to $Bi_2Te_3$ in the report of Park et al. [208],

forming a p-type material with an enhanced power factor of 4.26 mW·m⁻¹·K⁻². 

The research into thermoelectric materials enhancement through isovalent substitution has been a mechanism to control the carrier concentration while improving the electrical conductivity and Seebeck coefficient in TE materials. Before 1950, the conversion efficiency was less than 5%, while after 1990, this improved to 20% [209, 210]. It is considered that further improvement is still possible. For such reasons, this review is targeted to the contribution of the isovalent substitution to thermoelectric material performance from reports within the past few decades to illuminate the impact of the synthesis route on TE performance.

## 5    Conclusion

In conclusion, the system of isovalent substitution is an effective technique of doping to enhance the thermoelectric material performance through the distortion of the density of state via the formation of defects states, which serve as resonant levels. Unlike the conventional doping system, isovalent doping reveals a departure from the rigid band approximation, which is salient in improving the electron density of the state and eventually enhancing the Seebeck coefficient. 15% of the reviewed articles did not show a simultaneous increment in the electrical conductivity and the Seebeck coefficient. However, their power factor was enhanced while the thermal conductivity was reduced due to the isovalent dopants' inclusion. Most of the reviewed articles (75%) revealed simultaneous improvement in the Seebeck coefficient and electrical conductivity. Secondly, the electron mobility in most cases was enhanced due to controlled isovalent substitution. Therefore, it is shown that the system of isovalent substitution is an effective tool to enhance the power factor via decoupling the interplay between the Seebeck coefficient and the electrical conductivity.

In summary, this paper reviews MC's electronic and thermoelectric properties, emphasising the isovalent doping approach. Among these materials, n-type $Bi_2Te_3$ and p-type $Bi_{0.5}Sb_{1.5}Te_3$ stand tall with the highest thermoelectric figure of merit of approximately close to 1. These materials possess high electrical conductivity and a high Seebeck coefficient, leading to a high-power factor. However, the limiting factor in this regard is the high thermal conductivity. Therefore, innovative strategies are required to further reduce the existing MC's total thermal conductivity and their composites. If the current thermal conductivity values of the n-type $Bi_2Te_3$ and $Bi_{0.5}Sb_{1.5}Te_3$ can be reduced by half, the zT will be doubled. Doubling the existing zT values of the commercialised TE materials will revolutionise the energy sector.

### Declaration of conflicting interests

The authors declare no conflicting interests regarding the content of this article.

### References

[1]    Cullen, J. M.; Allwood, J. M. Theoretical efficiency limits for energy conversion devices. *Energy* **2010**, *35*, 2059–2069.

[2] Turney, D.; Fthenakis, V. Environmental impacts from the installation and operation of large-scale solar power plants. *Renew. Sustainable Energy Rev.* **2011**, *15*, 3261–3270.

[3] Nolas, J. S.; Sharp, J.; Goldsmid, H. J. *Thermoelectrics*: *Basic Principles and New Materials Developments*. Springer: Berlin, 2001.

[4] Tritt, T. M.; Subramanian, M. A. Thermoelectric materials, phenomena, and applications: A bird's eye view. *MRS Bull.* **2006**, *31*, 188–198.

[5] Snyder, G. J.; Toberer, E. S. Complex thermoelectric materials. *Nat. Mater.* **2008**, *7*, 105–114.

[6] Liu, W. D.; Yang, L.; Chen, Z. G. $Cu_2Se$ thermoelectrics: Property, methodology, and device. *Nano Today* **2020**, *35*, 100938.

[7] Rowe, D. M. *Thermoelectrics Handbook*: *Macro to Nano*. CRC Press: Boca Raton, **2006**.

[8] Han, C.; Sun, Q.; Li, Z.; Dou, S. X. Thermoelectric enhancement of different kinds of metal chalcogenides. *Adv. Energy Mater.* **2016**, *6*, 1600498.

[9] Yu, F. R.; Zhang, J. J.; Yu, D. L.; He, J. L.; Liu, Z. Y.; Xu, B.; Tian, Y. J. Enhanced thermoelectric figure of merit in nanocrystalline $Bi_2Te_3$ bulk. *J. Appl. Phys.* **2009**, *105*, 094303.

[10] Pei, Y. Z.; Wang, H.; Snyder, G. J. Band engineering of thermoelectric materials. *Adv. Mater.* **2012**, *24*, 6125–6135.

[11] Baláž, P.; Baláž, M.; Achimovičová, M.; Bujňáková, Z.; Dutková, E. Chalcogenide mechanochemistry in materials science: Insight into synthesis and applications (a review). *J. Mater. Sci.* **2017**, *52*, 11851–11890.

[12] Siddique, A. R. M.; Mahmud, S.; Van Heyst, B. A review of the state of the science on wearable thermoelectric power generators (TEGs) and their existing challenges. *Renew. Sustainable Energy Rev.* **2017**, *73*, 730–744.

[13] Nielsch, K.; Bachmann, J.; Kimling, J.; Böttner, H. Thermoelectric nanostructures: From physical model systems towards nanograined composites. *Adv. Energy Mater.* **2011**, *1*, 713–731.

[14] Li, Z.; Sun, Q.; Yao, X. D.; Zhu, Z. H.; Lu, G. Q. Semiconductor nanowires for thermoelectrics. *J. Mater. Chem.* **2012**, *22*, 22821–22831.

[15] He, J.; Liu, Y. F.; Funahashi, R. Oxide thermoelectrics: The challenges, progress, and outlook. *J. Mater. Res.* **2011**, *26*, 1762–1772.

[16] Jood, P.; Ohta, M. Hierarchical architecturing for layered thermoelectric sulfides and chalcogenides. *Materials (Basel)*. **2015**, *8*, 1124–1149.

[17] Dennler, G.; Chmielowski, R.; Jacob, S.; Capet, F.; Roussel, P.; Zastrow, S.; Nielsch, K.; Opahle, I.; Madsen, G. K. H. Are binary copper sulfides/selenides really new and promising thermoelectric materials? *Adv. Energy Mater.* **2014**, *4*, 1301581.

[18] Minnich, A. J.; Dresselhaus, M. S.; Ren, Z. F.; Chen, G. Bulk nanostructured thermoelectric materials: Current research and future prospects. *Energy Environ. Sci.* **2009**, *2*, 466–479.

[19] He, R.; Schierning, G.; Nielsch, K. Thermoelectric devices: A review of devices, architectures, and contact optimization. *Adv. Mater. Technol.* **2018**, *3*, 1700256.

[20] Kim, W.; Wang, R.; Majumdar, A. Nanostructuring expands thermal limits. *Nano Today* **2007**, *2*, 40–47.

[21] Li, L.; Liu, W. D.; Liu, Q. F.; Chen, Z. G. Multifunctional wearable thermoelectrics for personal thermal management. *Adv. Funct. Mater.* **2022**, *32*, 2200548.

[22] Chen, Z. G.; Liu, W. D. Thermoelectric coolers: Infinite potentials for finite localized microchip cooling. *J. Mater. Sci. Technol.* **2022**, *121*, 256–262.

[23] Hyland, M.; Hunter, H.; Liu, J.; Veety, E.; Vashaee, D. Wearable thermoelectric generators for human body heat harvesting. *Appl. Energy* **2016**, *182*, 518–524.

[24] Guo, L. K.; Lu, Q. Potentials of piezoelectric and thermoelectric technologies for harvesting energy from pavements. *Renew. Sustainable Energy Rev.* **2017**, *72*, 761–773.

[25] Bell, L. E. Cooling, heating, generating power, and recovering waste heat with thermoelectric systems. *Science* **2008**, *321*, 1457–1461.

[26] Yuan, J. F.; Zhu, R.; Li, G. Z. Self-powered electronic skin with multisensory functions based on thermoelectric conversion. *Adv. Mater. Technol.* **2020**, *5*, 2000419.

[27] Yuan, J. F.; Zhu, R. A fully self-powered wearable monitoring system with systematically optimized flexible thermoelectric generator. *Appl. Energy* **2020**, *271*, 115250.

[28] Kim, J.; Khan, S.; Wu, P.; Park, S.; Park, H.; Yu, C.; Kim, W. Self-charging wearables for continuous health monitoring. *Nano Energy* **2021**, *79*, 105419.

[29] Van Toan, N.; Tuoi, T. T. K.; Sui, H. T.; Trung, N. H.; Samat, K. F.; Ono, T. Ultra-flexible thermoelectric generator based on silicone rubber sheet and electrodeposited thermoelectric material for waste heat harvesting. *Energy Rep.* **2022**, *8*, 5026–5037.

[30] Le, T.; Mayaram, K.; Fiez, T. Efficient far-field radio frequency energy harvesting for passively powered sensor networks. *IEEE J. Solid-State Circuits* **2008**, *43*, 1287–1302.

[31] Ioffe, A. F. *Physics of Semiconductors*. Academic Press Inc.: New York, 1961.

[32] Datta, S. *Lessons from Nanoelectronics*: *A New Perspective on Transport*. World Scientific: Singapore, 2012.

[33] Vesely, F. J. *Computational Physics*: *An Introduction*. Springer: New York, 2001.

[34] Mohamad, A. A. *Lattice Boltzmann Method*: *Fundamentals and Engineering Applications with Computer Codes*. Springer: London, 2011.

[35] Mamur, H.; Üstüner, M. A.; Dilmaç, Ö. F.; Bhuiyan, M. R. A. Performance evaluation of $Bi_2Te_{3-x}Se_x$ ($0.10 \le x \le 1.80$) thermoelectric nanostructured materials. *Cleaner Chemical Engineering*, **2022**, *4*, 100063.

[36] Pineda, D. D.; Rezaniakolaei, A.; Brand, O.; Fedder, G. K.; Hierold, C.; Korvink, J. G. Tabata, O. *Thermoelectric Energy Conversion*: *Basic Concepts and Device Applications*. Wiley-VCH: Weinheim, 2017.

[37] Memon, S.; Mihreteab, M.; Katsura, T.; Radwan, A.; Zhang, S.; Serageldin, A. A.; Abo-Zahhad, E. M. Experimental and theoretical performance evaluation of parabolic trough mirror as a solar thermal concentrator to thermoelectric generators. *International Journal of Solar Thermal Vacuum Engineering* **2020**, *1*, 23–38.

[38] Poudel, B.; Hao, Q.; Ma, Y.; Lan, Y. C.; Minnich, A.; Yu, B.; Yan, X.; Wang, D. Z.; Muto, A.; Vashaee, D. et al. High-thermoelectric performance of nanostructured bismuth antimony telluride bulk alloys. *Science* **2008**, *320*, 634–638.

[39] Yavorsky, B. Y.; Hinsche, N. F.; Mertig, I.; Zahn, P. Electronic structure and transport anisotropy of $Bi_2Te_3$ and $Sb_2Te_3$. *Phys. Rev. B* **2011**, *84*, 165208.

[40] Richter, W.; Becker, C. R. Raman and far-infrared investigation of phonons in the rhombohedral $V_2$-$VI_3$ compounds $Bi_2Te_3$, $Bi_2Se_3$, $Sb_2Te_3$ and $Bi_2(Te_{1-x}Se_x)_3$ ($0<x<1$), $(Bi_{1-y}Sb_y)_2Te_3$ ($0<y<1$). *Phys. Status Solidi* **1977**, *84*, 619–628.

[41] Wang, H.; Zhu, J. J.; Zhu, J. M.; Chen, H. Y. Sonochemical method for the preparation of bismuth sulfide nanorods. *J. Phys. Chem. B* **2002**, *106*, 3848–3854.

[42] Harman, T. C.; Taylor, P. J.; Walsh, M. P.; LaForge, B. E. Quantum dot superlattice thermoelectric materials and devices. *Science* **2002**, *297*, 2229–2232.

[43] Zhao, L. D.; Lo, S. H.; Zhang, Y. S.; Sun, H.; Tan, G. J.; Uher, C.; Wolverton, C.; Dravid, V. P.; Kanatzidis, M. G. Ultralow thermal conductivity and high thermoelectric figure of merit in SnSe crystals. *Nature* **2014**, *508*, 373–377.

[44] Biswas, K.; He, J. Q.; Blum, I. D.; Wu, C. I.; Hogan, T. P.; Seidman, D. N.; Dravid, V. P.; Kanatzidis, M. G. High-performance bulk thermoelectrics with all-scale hierarchical architectures. *Nature* **2012**, *489*, 414–418.

[45] Venkatasubramanian, R.; Siivola, E.; Colpitts, T.; O'Quinn, B. Thin-film thermoelectric devices with high room-temperature figures of merit. *Nature* **2001**, *413*, 597–602.

[46] Xie, W. J.; Tang, X. F.; Yan, Y. G.; Zhang, Q. J.; Tritt, T. M. Unique nanostructures and enhanced thermoelectric performance of melt-spun BiSbTe alloys. *Appl. Phys. Lett.* **2009**, *94*, 102111.

[47] Salavati-Niasari, M.; Bazarganipour, M.; Davar, F. Hydrothermal synthesis and characterization of bismuth selenide nanorods via a co-reduction route. *Inorg. Chim. Acta* **2011**, *365*, 61–64.

[48] Batabyal, S. K.; Basu, C.; Das, A. R.; Sanyal, G. S. Solvothermal synthesis of bismuth selenide nanotubes. *Mater. Lett.* **2006**, *60*, 2582–2585.

[49] Yang, X. H.; Wang, X.; Zhang, Z. D. Synthesis and optical properties of single-crystalline bismuth selenide nanorods via a convenient route. *J. Cryst. Growth* **2005**, *276*, 566–570.

[50] Hu, P. F.; Cao, Y. L.; Jia, D. Z.; Wang, L. X. Selective synthesis of $Bi_2Se_3$ nanostructures by solvothermal reaction. *Mater. Lett.* **2010**, *64*, 493–496.

[51] Li, J.; Zhu, Y. C.; Du, J.; Zhang, J. H.; Qian, Y. T. Synthesis and shape evolution of bismuth selenide hollow nanospheres. *Solid State Commun.* **2008**, *147*, 36–40.

[52] Loor, M.; Bendt, G.; Schaumann, J.; Hagemann, U.; Heidelmann, M.; Wölper, C.; Schulz, S. Synthesis of $Sb_2Se_3$ and $Bi_2Se_3$ nanoparticles in ionic liquids at low temperatures and solid state structure of $[C_4C_1Im]_3[BiCl_6]$. *Z. Anorg. Allg. Chem.* **2017**, *643*, 60–68.

[53] Jin, R. C.; Sun, M. W.; Li, G. H. CNTs@C@$Bi_2Se_3$ composite as an improved-performance anode for lithium ion batteries. *Ceram. Int.* **2017**, *43*, 17093–17099.

[54] Harpeness, R.; Gedanken, A. Microwave-assisted synthesis of nanosized $Bi_2Se_3$. *New J. Chem.* **2003**, *27*, 1191–1193.

[55] Jiang, Y.; Zhu, Y. J.; Cheng, G. F. Synthesis of $Bi_2Se_3$ nanosheets by microwave heating using an ionic liquid. *Cryst. Growth Des.* **2006**, *6*, 2174–2176.

[56] Ramezani, M.; Sobhani-Nasab, A.; Davoodi, A. Bismuth selenide nanoparticles: Simple synthesis, characterization, and its light harvesting applications in the presence of novel precursor. *J. Mater. Sci. Mater. Electron.* **2015**, *26*, 5440–5445.

[57] Qiu, X. F.; Burda, C.; Fu, R. L.; Pu, L.; Chen, H. Y.; Zhu, J. J. Heterostructured $Bi_2Se_3$ nanowires with periodic phase boundaries. *J. Am. Chem. Soc.* **2004**, *126*, 16276–16277.

[58] Gedanken, A. Using sonochemistry for the fabrication of nanomaterials. *Ultrason. Sonochem.* **2004**, *11*, 47–55.

[59] Qiu, X. F.; Lou, Y. B.; Samia, A. C. S.; Devadoss, A.; Burgess, J. D.; Dayal, S.; Burda, C. PbTe nanorods by sonoelectrochemistry. *Angew. Chem., Int. Ed.* **2005**, *44*, 5855–5857.

[60] Larsson, N. Optical and structural properties of $Cu_xS$ quantum dots concerning $H_2O$/ethanol solvent ratio. **2013**.

[61] Lin, S. S.; Liao, C. N. Effect of ball milling and post treatment on crystal defects and transport properties of $Bi_2(Se, Te)_3$ compounds. *J. Appl. Phys.* **2011**, *110*, 093707.

[62] Jabar, B.; Mansoor, A.; Chen, Y. X.; Jamil, S.; Chen, S.; Liang, G. X.; Li, F.; Fan, P.; Zheng, Z. H. High thermoelectric performance of $Bi_xSb_{2-x}Te_3$ alloy achieved via structural manipulation under optimized heat treatment. *Chem. Eng. J.* **2022**, *435*, 135062.

[63] Lan, Y. C.; Minnich, A. J.; Chen, G.; Ren, Z. F. Enhancement of thermoelectric figure-of-merit by a bulk nanostructuring approach. *Adv. Funct. Mater.* **2010**, *20*, 357–376.

[64] Gharsallah, M.; Serrano-Sanchez, F. Nemes, N. M.; Martinez, J. L.; Alonso, J. A. Influence of doping and nanostructuration on n-type $Bi_2(Te_{0.8}Se_{0.2})_3$ alloys synthesized by arc melting. *Nanoscale Res. Lett.* **2017**, *12*, 47.

[65] Das, D.; Malik, K.; Deb, A. K.; Kulbachinskii, V. A.; Kytin, V. G.; Chatterjee, S.; Das, D.; Dhara, S.; Bandyopadhyay, S.; Banerjee, A. Tuning of thermoelectric properties with changing Se content in $Sb_2Te_3$. *Eur. Lett.* **2016**, *113*, 47004.

[66] Das, D.; Malik, K.; Deb, A. K.; Dhara, S.; Bandyopadhyay, S.; Banerjee, A. Defect induced structural and thermoelectric properties of $Sb_2Te_3$ alloy. *J. Appl. Phys.* **2015**, *118*, 045102.

[67] Kulbachinskii, V. A.; Dashevskii, Z. M.; Inoue, M.; Sasaki, M.; Negishi, H.; Gao, W. X.; Lostak, P.; Horak, J.; de Visser, A. Valence-band changes in $Sb_{2-x}In_xTe_3$ and $Sb_2Te_{3-y}Se_y$ by transport and Shubnikov-de Haas effect measurements. *Phys. Rev. B* **1995**, *52*, 10915–10922.

[68] Logan, R. A.; Peters, A. J. Impurity effects upon mobility in silicon. *J. Appl. Phys.* **1960**, *31*, 122–124.

[69] Hoang, K.; Mahanti, S. D. Electronic structure of Ga-, In-, and Tl-doped PbTe: A supercell study of the impurity bands. *Phys. Rev. B* **2008**, *78*, 085111.

[70] Jaworski, C. M.; Wiendlocha, B.; Jovovic, V.; Heremans, J. P. Combining alloy scattering of phonons and resonant electronic levels to reach a high thermoelectric figure of merit in PbTeSe and PbTeS alloys. *Energy Environ. Sci.* **2011**, *4*, 4155–4162.

[71] Heremans, J. P.; Jovovic, V.; Toberer, E. S.; Saramat, A.; Kurosaki, K.; Charoenphakdee, A.; Yamanaka, S.; Snyder, G. J. Enhancement of thermoelectric efficiency in PbTe by distortion of the electronic density of states. *Science* **2008**, *321*, 554–557.

[72] Heremans, J. P.; Wiendlocha, B.; Chamoire, A. M. Resonant levels in bulk thermoelectric semiconductors. *Energy Environ. Sci.* **2012**, *5*, 5510–5530.

[73] Jin, H.; Wiendlocha, B.; Heremans, J. P. P-type doping of elemental bismuth with indium, gallium and tin: A novel doping mechanism in solids. *Energy Environ. Sci.* **2015**, *8*, 2027–2040.

[74] Walukiewicz, W.; Shan, W.; Yu, K. M.; Ager III, J. W.; Haller, E. E.; Miotkowski, I.; Seong, M. J.; Alawadhi, H.; Ramdas, A. K. Interaction of localized electronic states with the conduction band: Band anticrossing in II-VI semiconductor ternaries. *Phys. Rev. Lett.* **2000**, *85*, 1552–1555.

[75] Pei, Y. Z.; Shi, X. Y.; Lalonde, A.; Wang, H.; Chen, L. D.; Snyder, G. J. Convergence of electronic bands for high performance bulk thermoelectrics. *Nature* **2011**, *473*, 66–69.

[76] Dresselhaus, M. S.; Chen, G.; Tang, M. Y.; Yang, R. G.; Lee, H.; Wang, D. Z.; Ren, Z. F.; Fleurial, J. P.; Gogna, P. New directions for low-dimensional thermoelectric materials. *Adv. Mater.* **2007**, *19*, 1043–1053.

[77] Yang, H. R.; Bahk, J. H.; Day, T.; Mohammed, A. M. S.; Snyder, G. J.; Shakouri, A.; Wu, Y. Enhanced thermoelectric properties in bulk nanowire heterostructure-based nanocomposites through minority carrier blocking. *Nano Lett.* **2015**, *15*, 1349–1355.

[78] Kanatzidis, M. G. Nanostructured thermoelectrics: The new paradigm? *Chem. Mater.* **2010**, *22*, 648–659.

[79] Son, J. S.; Choi, M. K.; Han, M. K.; Park, K.; Kim, J. Y.; Lim, S. J.; Oh, M.; Kuk, Y.; Park, C.; Kim, S. J. et al. n-Type nanostructured thermoelectric materials prepared from chemically synthesized ultrathin $Bi_2Te_3$ nanoplates. *Nano Lett.* **2012**, *12*, 640–647.

[80] Zhang, G. Q.; Kirk, B.; Jauregui, L. A.; Yang, H. R.; Xu, X. F.; Chen, Y. P.; Wu, Y. Rational synthesis of ultrathin n-type $Bi_2Te_3$ nanowires with enhanced thermoelectric properties. *Nano Lett.* **2012**, *12*, 56–60.

[81] Han, G.; Chen, Z. G.; Yang, L.; Hong, M.; Drennan, J.; Zou, J. Rational design of $Bi_2Te_3$ polycrystalline whiskers for thermoelectric applications. *ACS Appl. Mater. Interfaces* **2015**, *7*, 989–995.

[82] Fang, H. Y.; Yang, H. R.; Wu, Y. Thermoelectric properties of silver telluride-bismuth telluride nanowire heterostructure synthesized by site-selective conversion. *Chem. Mater.* **2014**, *26*, 3322–3327.

[83] Fang, H. Y.; Feng, T. L.; Yang, H. R.; Ruan, X. L.; Wu, Y. Synthesis and thermoelectric properties of compositional-modulated lead telluride-bismuth telluride nanowire heterostructures. *Nano Lett.* **2013**, *13*, 2058–2063.

[84] Xie, W. J.; Tang, X. F.; Yan, Y. G.; Zhang, Q. J.; Tritt, T. M. High thermoelectric performance BiSbTe alloy with unique low-dimensional structure. *J. Appl. Phys.* **2009**, *105*, 113713.

[85] Fusa, M.; Yamamoto, N.; Hasezaki, K. Measurement of Seebeck coefficient and conductive behaviors of $Bi_2Te_{3-x}Se_x$ ($x = 0.15–0.6$) thermoelectric semiconductors without harmful dopants. *Mater. Trans.* **2014**, *55*, 942–946.

[86] Lowhorn, N. D.; Wong-Ng, W.; Lu, Z. Q.; Martin, J.; Green, M. L.; Bonevich, J. E.; Thomas, E. L.; Dilley, N. R.; Sharp, J. Development of a Seebeck coefficient standard reference material™. *J. Mater. Res.* **2011**, *26*, 1983–1992.

[87] Benday, N. S.; Dryden, D. M.; Kornbluth, K.; Stroeve, P. A temperature-variant method for performance modeling and economic analysis of thermoelectric generators: Linking material properties to real-world conditions. *Appl. Energy* **2017**, *190*, 764–771.

[88] Puyet, M.; Dauscher, A.; Lenoir, B.; Bellouard, C.; Stiewe, C.; Müller, E.; Hejtmanek, J.; Tobola, J. Influence of Ni on the thermoelectric properties of the partially filled calcium skutterudites $Ca_yCo_{4-x}Ni_xSb_{12}$. *Phys. Rev. B* **2007**, *75*, 245110.

[89] Puyet, M.; Dauscher, A.; Lenoir, B.; Dehmas, M.; Stiewe, C.; Müller, E.; Hejtmanek, J. Beneficial effect of Ni substitution on the thermoelectric properties in partially filled $Ca_yCo_{4-x}Ni_xSb_{12}$ skutterudites. *J. Appl. Phys.* **2005**, *97*, 083712.

[90] Qiu, P. F.; Yang, J.; Liu, R. H.; Shi, X.; Huang, X. Y.; Snyder, G. J.; Zhang, W.; Chen, L. D. High-temperature electrical and thermal transport properties of fully filled skutterudites $RFe_4Sb_{12}$(R=Ca, Sr, Ba, La, Ce, Pr, Nd, Eu, and Yb). *J. Appl. Phys.* **2011**, *109*, 063713.

[91] Sakurada, S.; Shutoh, N. Effect of Ti substitution on the thermoelectric properties of (Zr, Hf)NiSn half-Heusler compounds. *Appl. Phys. Lett.* **2005**, *86*, 082105.

[92] Shen, Q.; Chen, L.; Goto, T.; Hirai, T.; Yang, J.; Meisner, G. P.; Uher, C. Effects of partial substitution of Ni by Pd on the thermoelectric properties of ZrNiSn-based half-Heusler compounds. *Appl. Phys. Lett.* **2001**, *79*, 4165–4167.

[93] Katayama, T.; Kim, S. W.; Kimura, Y.; Mishima, Y. The effects of quaternary additions on thermoelectric properties of TiNiSn-based half-Heusler alloys. *J. Electron. Mater.* **2003**, *32*, 1160–1165.

[94] Zaitsev, V. K.; Fedorov, M. I.; Gurieva, E. A.; Eremin, I. S.; Konstantinov, P. P.; Samunin, A. Y.; Vedernikov, M. V. Highly effective $Mg_2Si_{1-x}Sn_x$ thermoelectrics. *Phys. Rev. B* **2006**, *74*, 045207.

[95] Bux, S. K.; Yeung, M. T.; Toberer, E. S.; Snyder, G. J.; Kaner, R. B.; Fleurial, J. P. Mechanochemical synthesis and thermoelectric properties of high quality magnesium silicide. *J. Mater. Chem.* **2011**, *21*, 12259–12266.

[96] Xu, G. J.; Funahashi, R.; Shikano, M.; Matsubara, I.; Zhou, Y. Q. Thermoelectric properties of the Bi- and Na-substituted $Ca_3Co_4O_9$ system. *Appl. Phys. Lett.* **2002**, *80*, 3760–3762.

[97] Jood, P.; Peleckis, G.; Wang, X. L.; Dou, S. X. Thermoelectric properties of $Ca_3Co_4O_9$ and $Ca_{2.8}Bi_{0.2}Co_4O_9$ thin films in their island formation mode. *J. Mater. Res.* **2013**, *28*, 1932–1939.

[98] Tsubota, T.; Ohtaki, M.; Eguchi, K.; Arai, H. Thermoelectric properties of Al-doped ZnO as a promising oxide material for high-temperature thermoelectric conversion. *J. Mater. Chem.* **1997**, *7*, 85–90.

[99] Misture, S.; Edwards, D. High-temperature oxide thermoelectrics. *Am. Ceram. Soc. Bull.* **2012**, *91*, 24–27.

[100] Musah, J. D.; Xiao, Y. J.; Ilyas, A. M.; Novak, T. G.; Jeon, S.; Arava, C.; Novikov, S. V.; Nikulin, D. S.; Xu, W.; Liu, L. Y. et al. Simultaneous enhancement of thermopower and electrical conductivity through isovalent substitution of cerium in bismuth selenide thermoelectric materials. *ACS Appl. Mater. Interfaces* **2019**, *11*, 44026–44035.

[101] Eshelby, J. D. The continuum theory of lattice defects. *Solid State Phys.* **1956**, *3*, 79–144.

[102] Musah, J. D.; Ilyas, A. M.; Novitskii, A.; Serhiienko, I.; Egbo, K. O.; Saianand, G.; Khovaylo, V.; Kwofie, S.; Yu, K. M.; Roy, V. A. L. Effective decoupling of Seebeck coefficient and the electrical conductivity through isovalent substitution of erbium in bismuth selenide thermoelectric material. *J. Alloys Compd.* **2020**, *857*, 157559.

[103] Wu, F.; Song, H. Z.; Jia, J. F.; Hu, X. Effects of Ce, Y, and Sm doping on the thermoelectric properties of $Bi_2Te_3$ alloy. *Prog. Nat. Sci. Mater. Int.* **2013**, *23*, 408–412.

[104] Lee, K. H.; Kim, H. S.; Kim, M.; Roh, J. W.; Lim, J. H.; Kim, W. J.; Kim, S. I.; Lee, W. Isovalent sulfur substitution to induce a simultaneous increase in the effective mass and weighted mobility of a p-type Bi-Sb-Te alloy: An approach to enhance the thermoelectric performance over a wide temperature range. *Acta Mater.* **2021**, *205*, 116578.

[105] Vaney, J. B.; Delaizir, G.; Wiendlocha, B.; Tobola, J.; Alleno, E.; Piarristeguy, A.; Gonçalves, A. P.; Gendarme, C.; Malaman, B.; Dauscher, A. et al. Effect of isovalent substitution on the electronic structure and thermoelectric properties of the solid solution $\alpha$-$As_2Te_{3-x}Se_x$ ($0 \leq x \leq 1.5$). *Inorg. Chem.* **2017**, *56*, 2248–2257.

[106] Devender; Gehring, P.; Gaul, A.; Hoyer, A.; Vaklinova, K.; Mehta, R. J.; Burghard, M.; Borca-Tasciuc, T.; Singh, D. J.; Kern, K. et al. Harnessing topological band effects in bismuth telluride selenide for large enhancements in thermoelectric properties through isovalent doping. *Adv. Mater.* **2016**, *28*, 6436–6441.

[107] Shi, H. L.; Parker, D.; Du, M. H.; Singh, D. J. Connecting thermoelectric performance and topological-insulator behavior: $Bi_2Te_3$ and $Bi_2Te_2Se$ from first principles. *Phys. Rev. Appl.* **2015**, *3*, 014004.

[108] Neupane, M.; Xu, S. Y.; Wray, L. A.; Petersen, A.; Shankar, R.; Alidoust, N.; Liu, C.; Fedorov, A.; Ji, H.; Allred, J. M. et al. Topological surface states and Dirac point tuning in ternary topological insulators. *Phys. Rev. B* **2012**, *85*, 235406.

[109] Xu, S. Y.; Xia, Y.; Wray, L. A.; Jia, S.; Meier, F.; Dil, J. H.; Osterwalder, J.; Slomski, B.; Bansil, A.; Lin, H. et al. Topological phase transition and texture inversion in a tunable topological insulator. *Science* **2011**, *332*, 560–564.

[110] Gehring, P.; Benia, H. M.; Weng, Y.; Dinnebier, R.; Ast, C. R.; Burghard, M.; Kern, K. A natural topological insulator. *Nano Lett.* **2013**, *13*, 1179–1184.

[111] Musah, J. D.; Guo, C.; Novitskii, A.; Serhiienko, I.; Adesina, A. E.; Khovaylo, V.; Wu, C. L.; Zapien, J. A.; Roy, V. A. L. Ultralow thermal conductivity in dual-doped n-type $Bi_2Te_3$ material for enhanced thermoelectric properties. *Adv. Electron. Mater.* **2021**, *7*, 2000910.

[112] Liu, S.; Peng, N.; Zhou, C. J.; Bai, Y.; Tang, S.; Ma, D. Y.; Ma, F.; Xu, K. W. Fabrication of $Bi_2Te_{3-x}Se_x$ nanowires with tunable chemical compositions and enhanced thermoelectric properties. *Nanotechnology* **2017**, *28*, 085601.

[113] Soni, A.; Zhao, Y. Y.; Yu, L. G.; Aik, M. K. K.; Dresselhaus, M. S.; Xiong, Q. H. Enhanced thermoelectric properties of solution grown $Bi_2Te_{3-x}Se_x$ nanoplatelet composites. *Nano Lett.* **2012**, *12*, 1203–1209.

[114] Miller, G. R.; Li, C. Y. Evidence for the existence of antistructure defects in bismuth telluride by density measurements. *J. Phys. Chem. Solids* **1965**, *26*, 173–177.

[115] Shewmon, P. G. *Diffusion in Solids*. McGraw-Hill: New York, 1963.

[116] Hong, M.; Chen, Z. G.; Zou, J. Fundamental and progress of $Bi_2Te_3$-based thermoelectric materials. *Chin. Phys. B* **2018**, *27*, 048403.

[117] Wiese, J. R.; Muldawer, L. Lattice constants of $Bi_2Te_3$-$Bi_2Se_3$ solid solution alloys. *J. Phys. Chem. Solids* **1960**, *15*, 13–16.

[118] Drabble, J. R.; Goodman, C. H. L. Chemical bonding in bismuth telluride. *J. Phys. Chem. Solids* **1958**, *5*, 142–144.

[119] Horák, J.; Starý, Z.; Lošťák, P.; Pancíř, J. Anti-site defects in n-$Bi_2Se_3$ crystals. *J. Phys. Chem. Solids* **1990**, *51*, 1353–1360.

[120] Schultz, J. M.; McHugh, J. P.; Tiller, W. A. Effects of heavy deformation and annealing on the electrical properties of $Bi_2Te_3$. *J. Appl. Phys.* **1962**, *33*, 2443–2450.

[121] Li, D.; Qin, X. Y.; Dou, Y. C.; Li, X. Y.; Sun, R. R.; Wang, Q. Q.; Li, L. L.; Xin, H. X.; Wang, N.; Wang, N. N.; et al. Thermoelectric properties of hydrothermally synthesized $Bi_2Te_{3-x}Se_x$ nanocrystals. *Scripta Materialia* **2012**, *67*, 161–164.

[122] Srinivasan, R.; Gothard, N.; Spowart, J. Improvement in thermoelectric properties of an n-type bismuth telluride ($Bi_2Se_{0.3}Te_{2.7}$) due to texture development and grain refinement during hot deformation. *Mater. Lett.* **2010**, *64*, 1772–1775.

[123] Yan, X.; Poudel, B.; Ma, Y.; Liu, W. S.; Joshi, G.; Wang, H.; Lan, Y. C.; Wang, D. Z.; Chen, G.; Ren, Z. F. Experimental studies on anisotropic thermoelectric properties and structures of n-type $Bi_2Te_{2.7}Se_{0.3}$. *Nano Lett.* **2010**, *10*, 3373–3378.

[124] Kim, C.; Kim, D. H.; Kim, J. S.; Han, Y. S.; Chung, J. S.; Kim, H. A study of the synthesis of bismuth tellurium selenide nanocompounds and procedures for improving their thermoelectric performance. *J. Alloys Compd.* **2011**, *509*, 9472–9478.

[125] Carlton, C. E.; Kuryak, C. A.; Liu, W. S.; Ren, Z. F.; Chen, G.; Shao-Horn, Y. Disordered stoichiometric nanorods and ordered off-stoichiometric nanoparticles in n-type thermoelectric Bi$_2$Te$_{2.7}$Se$_{0.3}$. *J. Appl. Phys*. **2012**, *112*, 093518.

[126] Hu, L. P.; Zhu, T. J.; Liu, X. H.; Zhao, X. B. Point defect engineering of high-performance bismuth-telluride-based thermoelectric materials. *Adv. Funct. Mater*. **2014**, *24*, 5211–5218.

[127] Keawprak, N.; Lao-Ubol, S.; Eamchotchawalit, C.; Sun, Z. M. Thermoelectric properties of Bi$_2$Se$_x$Te$_{3-x}$ prepared by Bridgman method. *J. Alloys Compd*. **2011**, *509*, 9296–9301.

[128] Nozariasbmarz, A.; Krasinski, J. S.; Vashaee, D. n-Type bismuth telluride nanocomposite materials optimization for thermoelectric generators in wearable applications. *Materials (Basel)*. **2019**, *12*, 1529.

[129] Lu, X.; Yao, W.; Wang, G. W.; Zhou, X. Y.; Morelli, D.; Zhang, Y. S.; Chu, H.; Hui, S.; Uher, C. Band structure engineering in highly degenerate tetrahedrites through isovalent doping. *J. Mater. Chem. A* **2016**, *4*, 17096–17103.

[130] Sk, R.; Shirolkar, M. M.; Dhara, B.; Kulkarni, S.; Deshpande, A. Enhancing the thermopower and tuning the resistivity in Bi$_2$Se$_3$ with Fe-doping. *Chem. Phys. Lett*. **2015**, *638*, 94–98.

[131] Sun, G. L.; Qin, X. Y.; Li, D.; Zhang, J.; Ren, B. J.; Zou, T. H.; Xin, H. X.; Paschen, S. B.; Yan, X. L. Enhanced thermoelectric performance of n-type Bi$_2$Se$_3$ doped with Cu. *J. Alloys Compd*. **2015**, *639*, 9–14.

[132] Cho, H.; Kim, J. H.; Back, S. Y.; Ahn, K.; Rhyee, J. S.; Park, S. D. Enhancement of thermoelectric properties in CuI-doped Bi$_2$Te$_{2.7}$Se$_{0.3}$ by hot-deformation. *J. Alloys Compd*. **2018**, *731*, 531–536.

[133] Vaško, A.; Tichý, L.; Horák, J.; Weissenstein, J. Amphoteric nature of copper impurities in Bi$_2$Se$_3$ crystals. *Appl. Phys*. **1974**, *5*, 217–221.

[134] Majumdar, A. Thermoelectricity in semiconductor nanostructures. *Science* **2004**, *303*, 777–779.

[135] Zhang, X.; Zhao, L. D. Thermoelectric materials: Energy conversion between heat and electricity. *J. Mater*. **2015**, *1*, 92–105.

[136] Liao, B. L.; Chen, G. Nanocomposites for thermoelectrics and thermal engineering. *MRS Bull*. **2015**, *40*, 746–752.

[137] He, J. Q.; Kanatzidis, M. G.; Dravid, V. P. High performance bulk thermoelectrics via a panoscopic approach. *Mater. Today* **2013**, *16*, 166–176.

[138] Zhao, L. D.; Dravid, V. P.; Kanatzidis, M. G. The panoscopic approach to high performance thermoelectrics. *Energy Environ. Sci*. **2014**, *7*, 251–268.

[139] Heinrich, C. P.; Day, T. W.; Zeier, W. G.; Snyder, G. J.; Tremel, W. Effect of isovalent substitution on the thermoelectric properties of the Cu$_2$ZnGeSe$_{4-x}$S$_x$ series of solid solutions. *J. Am. Chem. Soc*. **2014**, *136*, 442–448.

[140] Chmielowski, R.; Bhattacharya, S.; Jacob, S.; Péré, D.; Jacob, A.; Moriya, K.; Delatouche, B.; Roussel, P.; Madsen, G.; Dennler, G. Strong reduction of thermal conductivity and enhanced thermoelectric properties in CoSbS$_{1-x}$Se$_x$ paracostibite. *Sci. Rep*. **2017**, *7*, 46630.

[141] Wu, C. F.; Wei, T. R.; Li, J. F. Enhancing average ZT in pristine PbSe by over-stoichiometric Pb addition. *APL Mater*. **2016**, *4*, 104801.

[142] Lee, Y.; Lo, S. H.; Chen, C. Q.; Sun, H.; Chung, D. Y.; Chasapis, T. C.; Uher, C.; Dravid, V. P.; Kanatzidis, M. G. Contrasting role of antimony and bismuth dopants on the thermoelectric performance of lead selenide. *Nat. Commun*. **2014**, *5*, 3640.

[143] Liu, W. S.; Guo, C. F.; Yao, M. L.; Lan, Y. C.; Zhang, H.; Zhang, Q.; Chen, S.; Opeil, C. P.; Ren, Z. F. Bi$_2$S$_3$ nanonetwork as precursor for improved thermoelectric performance. *Nano Energy* **2014**, *4*, 113–122.

[144] Yu, F. R.; Xu, B.; Zhang, J. J.; Yu, D. L.; He, J. L.; Liu, Z. Y.; Tian, Y. J. Structural and thermoelectric characterizations of high pressure sintered nanocrystalline Bi$_2$Te$_3$ bulks. *Mater. Res. Bull*. **2012**, *47*, 1432–1437.

[145] Zhao, L. D.; Zhang, B. P.; Li, J. F.; Zhang, H. L.; Liu, W. S. Enhanced thermoelectric and mechanical properties in textured n-type Bi$_2$Te$_3$ prepared by spark plasma sintering. *Solid State Sci*. **2008**, *10*, 651–658.

[146] Park, K.; Ahn, K.; Cha, J.; Lee, S.; Chae, S. I.; Cho, S. P.; Ryee, S.; Im, J.; Lee, J.; Park, S. D. et al. Extraordinary off-stoichiometric bismuth telluride for enhanced n-type thermoelectric power factor. *J. Am. Chem. Soc*. **2016**, *138*, 14458–14468.

[147] Zhang, Q.; Liao, B. L.; Lan, Y. C.; Lukas, K.; Liu, W. S.; Esfarjani, K.; Opeil, C.; Broido, D.; Chen, G.; Ren, Z. F. High thermoelectric performance by resonant dopant indium in nanostructured SnTe. *Proc. Natl. Acad. Sci. USA* **2013**, *110*, 13261–13266.

[148] Zhao, L. D.; He, J. Q.; Wu, C. I.; Hogan, T. P.; Zhou, X. Y.; Uher, C.; Dravid, V. P.; Kanatzidis, M. G. Thermoelectrics with earth abundant elements: High performance p-type PbS nanostructured with SrS and CaS. *J. Am. Chem. Soc*. **2012**, *134*, 7902–7912.

[149] Yu, B.; Liu, W. S.; Chen, S.; Wang, H.; Wang, H. Z.; Chen, G.; Ren, Z. F. Thermoelectric properties of copper selenide with ordered selenium layer and disordered copper layer. *Nano Energy* **2012**, *1*, 472–478.

[150] Jiang, Q. H.; Yan, H. X.; Khaliq, J.; Shen, Y.; Simpson, K.; Reece, M. J. Enhancement of thermoelectric properties by atomic-scale percolation in digenite Cu$_x$S. *J. Mater. Chem. A* **2014**, *2*, 9486–9489.

[151] Ali, Z.; Butt, S.; Cao, C. B.; Butt, F. K.; Tahir, M.; Tanveer, M.; Aslam, I.; Rizwan, M.; Idrees, F.; Khalid, S. Thermochemically evolved nanoplatelets of bismuth selenide with enhanced thermoelectric figure of merit. *AIP Adv*. **2014**, *4*, 117129.

[152] Kang, Y. L.; Zhang, Q.; Fan, C. Z.; Hu, W. P.; Chen, C.; Zhang, L.; Yu, F. R.; Tian, Y. J.; Xu, B. High pressure synthesis and thermoelectric properties of polycrystalline Bi$_2$Se$_3$. *J. Alloys Compd*. **2017**, *700*, 223–227.

[153] Tan, Q.; Li, J. F. Thermoelectric properties of Sn-S bulk materials prepared by mechanical alloying and spark plasma sintering. *J. Electron. Mater*. **2014**, *43*, 2435–2439.

[154] Shi, X.; Cho, J. Y.; Salvador, J. R.; Yang, J. H.; Wang, H. Thermoelectric properties of polycrystalline In$_4$Se$_3$ and In$_4$Te$_3$. *Appl. Phys. Lett*. **2010**, *96*, 162108.

[155] Wan, C. L.; Gu, X. K.; Dang, F.; Itoh, T.; Wang, Y. F.; Sasaki, H.; Kondo, M.; Koga, K.; Yabuki, K.; Snyder, G. J. et al. Flexible n-type thermoelectric materials by organic intercalation of layered transition metal dichalcogenide TiS$_2$. *Nat. Mater*. **2015**, *14*, 622–627.

[156] Liu, W. S.; Lukas, K. C.; McEnaney, K.; Lee, S.; Zhang, Q.; Opeil, C. P.; Chen, G.; Ren, Z. F. Studies on the Bi$_2$Te$_3$-Bi$_2$Se$_3$-Bi$_2$S$_3$ system for mid-temperature thermoelectric energy conversion. *Energy Environ. Sci*. **2013**, *6*, 552–560.

[157] Liu, D. W.; Li, J. F.; Chen, C.; Zhang, B. P. Effects of SiC nanodispersion on the thermoelectric properties of p-type and n-type Bi$_2$Te$_3$-based alloys. *J. Electron. Mater*. **2011**, *40*, 992–998.

[158] Li, H.; Cai, K. F.; Du, Y.; Wang, H. F.; Shen, S. Z.; Li, X. L.; Wang, Y. Y.; Zhou, C. W. Preparation and thermoelectric properties of AgPb$_{18}$SbTe$_{20-x}$Se$_x$ ($x$ =1, 2, 4) materials. *Curr. Appl. Phys*. **2012**, *12*, 188–192.

[159] Poudeu, P. F. P.; D'Angelo, J.; Kong, H. J.; Downey, A.; Short, J. L.; Pcionek, R.; Hogan, T. P.; Uher, C.; Kanatzidis, M. G. Nanostructures versus solid solutions: Low lattice thermal conductivity and enhanced thermoelectric figure of merit in Pb$_{9.6}$Sb$_{0.2}$Te$_{10-x}$Se$_x$ bulk materials. *J. Am. Chem. Soc*. **2006**, *128*, 14347–14355.

[160] Hong, M.; Chasapis, T. C.; Chen, Z. G.; Yang, L.; Kanatzidis, M. G.; Snyder, G. J.; Zou, J. n-Type Bi$_2$Te$_{3-x}$Se$_x$ nanoplates with enhanced thermoelectric efficiency driven by wide-frequency phonon scatterings and synergistic carrier scatterings. *ACS Nano* **2016**, *10*, 4719–4727.

[161] Ginting, D.; Lin, C. C.; Rathnam, L.; Yun, J. H.; Yu, B. K.; Kim, S. J.; Rhyee, J. S. High thermoelectric performance due to nano-inclusions and randomly distributed interface potentials in N-type (PbTe$_{0.93-x}$Se$_{0.07}$Cl$_x$)$_{0.93}$(PbS)$_{0.07}$ composites. *J. Mater. Chem. A* **2017**, *5*, 13535–13543.

[162] Banik, A.; Biswas, K. Lead-free thermoelectrics: Promising thermoelectric performance in p-type SnTe$_{1-x}$Se$_x$ system. *J. Mater. Chem. A* **2014**, *2*, 9620–9625.

[163] Zhou, Y. F.; Li, X. Y.; Bai, S. Q.; Chen, L. D. Comparison of space- and ground-grown $Bi_2Se_{0.21}Te_{2.79}$ thermoelectric crystals. *J. Cryst. Growth* **2010**, *312*, 775–780.

[164] Hu, L. P.; Liu, X. H.; Xie, H. H.; Shen, J. J.; Zhu, T. J.; Zhao, X. B. Improving thermoelectric properties of n-type bismuth-telluride-based alloys by deformation-induced lattice defects and texture enhancement. *Acta Mater.* **2012**, *60*, 4431–4437.

[165] Shin, W. H.; Roh, J. W.; Ryu, B.; Chang, H. J.; Kim, H. S.; Lee, S.; Seo, W. S.; Ahn, K. Enhancing thermoelectric performances of bismuth antimony telluride via synergistic combination of multiscale structuring and band alignment by $FeTe_2$ incorporation. *ACS Appl. Mater. Interfaces* **2018**, *10*, 3689–3698.

[166] Lan, Y. C.; Poudel, B.; Ma, Y.; Wang, D. Z.; Dresselhaus, M. S.; Chen, G.; Ren, Z. F. Structure study of bulk nanograined thermoelectric bismuth antimony telluride. *Nano Lett.* **2009**, *9*, 1419–1422.

[167] Zhu, T. J.; Xu, Z. J.; He, J.; Shen, J. J.; Zhu, S.; Hu, L. P.; Tritt, T. M.; Zhao, X. B. Hot deformation induced bulk nanostructuring of unidirectionally grown p-type $(Bi,Sb)_2Te_3$ thermoelectric materials. *J. Mater. Chem. A* **2013**, *1*, 11589–11594.

[168] Kim, S. I.; Lee, K. H.; Mun, H. A.; Kim, H. S.; Hwang, S. W.; Roh, J. W.; Yang, D. J.; Shin, W. H.; Li, X. S.; Lee, Y. H. et al. Dense dislocation arrays embedded in grain boundaries for high-performance bulk thermoelectrics. *Science* **2015**, *348*, 109–114.

[169] Li, H. Y.; Jing, H. Y.; Han, Y. D.; Lu, G. Q.; Xu, L. Y. Effects of mechanical alloying process and sintering methods on the microstructure and thermoelectric properties of bulk $Bi_{0.5}Sb_{1.5}Te_3$ alloy. *Intermetallics* **2013**, *43*, 16–23.

[170] Luo, Y. B.; Yang, J. Y.; Jiang, Q. H.; Fu, L. W.; Xiao, Y.; Li, W. X.; Zhang, D.; Zhou, Z. W.; Cheng, Y. D. Melting and solidification of bismuth antimony telluride under a high magnetic field: A new route to high thermoelectric performance. *Nano Energy* **2015**, *15*, 709–718.

[171] Jiang, Q. H.; Yan, H. X.; Khaliq, J.; Ning, H. P.; Grasso, S.; Simpson, K.; Reece, M. J. Large ZT enhancement in hot forged nanostructured p-type $Bi_{0.5}Sb_{1.5}Te_3$ bulk alloys. *J. Mater. Chem. A* **2014**, *2*, 5785–5790.

[172] Zhu, W. T.; Zhao, W. Y.; Zhou, H. Y.; Yu, J.; Tang, D. G.; Liu, Z. Y.; Zhang, Q. J. Cost-efficient preparation and enhanced thermoelectric performance of $Bi_{0.48}Sb_{1.52}Te_3$ bulk materials with micro- and nanostructures. *J. Electron. Mater.* **2014**, *43*, 1768–1774.

[173] Wu, F.; Shi, W. Y.; Hu, X. Preparation and thermoelectric properties of flower-like nanoparticles of Ce-doped $Bi_2Te_3$. *Electron. Mater. Lett.* **2015**, *11*, 127–132.

[174] Shen, J. J.; Zhu, T. J.; Zhao, X. B.; Zhang, S. N.; Yang, S. H.; Yin, Z. Z. Recrystallization induced *in situ* nanostructures in bulk bismuthantimony tellurides: A simple top down route and improved thermoelectric properties. *Energy Environ. Sci.* **2010**, *3*, 1519–1523.

[175] Xu, Z. J.; Hu, L. P.; Ying, P. J.; Zhao, X. B.; Zhu, T. J. Enhanced thermoelectric and mechanical properties of zone melted p-type $(Bi,Sb)_2Te_3$ thermoelectric materials by hot deformation. *Acta Mater.* **2015**, *84*, 385–392.

[176] Musah, J. D.; Liu, L. L.; Guo, C.; Novitskii, A.; Ilyas, A. O.; Serhiienko, I.; Khovaylo, V.; Roy, V. A. L.; Wu, C. M. L. Enhanced thermoelectric performance of bulk bismuth selenide: Synergistic effect of indium and antimony co-doping. *ACS Sustainable Chem. Eng.* **2022**, *10*, 3862–3871.

[177] Girard, S. N.; He, J. Q.; Zhou, X. Y.; Shoemaker, D.; Jaworski, C. M.; Uher, C.; Dravid, V. P.; Heremans, J. P.; Kanatzidis, M. G. High performance Na-doped PbTe-PbS thermoelectric materials: Electronic density of states modification and shape-controlled nanostructures. *J. Am. Chem. Soc.* **2011**, *133*, 16588–16597.

[178] Li, C. W.; Ma, J.; Cao, H. B.; May, A. F.; Abernathy, D. L.; Ehlers, G.; Hoffmann, C.; Wang, X.; Hong, T.; Huq, A. et al. Anharmonicity and atomic distribution of SnTe and PbTe thermoelectrics. *Phys. Rev. B* **2014**, *90*, 214303.

[179] Skelton, J. M.; Parker, S. C.; Togo, A.; Tanaka, I.; Walsh, A.

[180] Chen, Z. W.; Ge, B. H.; Li, W.; Lin, S. Q.; Shen, J. W.; Chang, Y. J.; Hanus, R.; Snyder, G. J.; Pei, Y. Z. Vacancy-induced dislocations within grains for high-performance PbSe thermoelectrics. *Nat. Commun.* **2017**, *8*, 13828.

[181] Shi, Y.; Tang, Y.; Liu, K.; Zhong, S.; Chen, S.; Yu, L.; Wu, J.; Zhang, Q.; Su, X.; Tang, X. Modulating the valence of Ga and the deep level impurity for high thermoelectric performance of n-type $Pb_{0.98}Ga_{0.02}Te_{1-x}Se_x$ compounds. *Mater. Today Phys.* **2022**, *27*, 100766.

[182] Wei, T. R.; Qin, Y. T.; Deng, T. T.; Song, Q. F.; Jiang, B. B.; Liu, R. H.; Qiu, P. F.; Shi, X.; Chen, L. D. Copper chalcogenide thermoelectric materials. *Sci. China Mater.* **2019**, *62*, 8–24.

[183] Tippireddy, S.; Powell, A. V.; Wong, T. K. S. High-performance low-cost sulfide/selenide thermoelectric devices. In *Sulfide and Selenide Based Materials for Emerging Applications*. Dalapati, G.; Wong, T. S.; Kundu, S.; Chakraborty, A.; Zhuk, S., Eds.; Elsevier: Amsterdam, 2022; pp 329–376.

[184] Zhao, K. P.; Liu, K.; Yue, Z. M.; Wang, Y. C.; Song, Q. F.; Li, J.; Guan, M. J.; Xu, Q.; Qiu, P. F.; Zhu, H. et al. Are $Cu_2Te$-based compounds excellent thermoelectric materials? *Adv. Mater.* **2019**, *31*, 1903480.

[185] Qin, B. C.; Wang, D. Y.; Liu, X. X.; Qin, Y. X.; Dong, J. F.; Luo, J. F.; Li, J. W.; Liu, W.; Tan, G. J.; Tang, X. F. et al. Power generation and thermoelectric cooling enabled by momentum and energy multiband alignments. *Science* **2021**, *373*, 556–561.

[186] Zhang, R.; Pei, J.; Han, Z. J.; Wu, Y.; Zhao, Z.; Zhang, B. P. Optimal performance of $Cu_{1.8}S_{1-x}Te_x$ thermoelectric materials fabricated via high-pressure process at room temperature. *J. Adv. Ceram.* **2020**, *9*, 535–543.

[187] Byeon, D.; Sobota, R.; Delime-Codrin, K.; Choi, S.; Hirata, K.; Adachi, M.; Kiyama, M.; Matsuura, T.; Yamamoto, Y.; Matsunami, M. et al. Discovery of colossal seebeck effect in metallic $Cu_2Se$. *Nat. Commun.* **2019**, *10*, 72.

[188] Li, W.; Lin, S. Q.; Zhang, X. Y.; Chen, Z. W.; Xu, X. F.; Pei, Y. Z. Thermoelectric properties of $Cu_2SnSe_4$ with intrinsic vacancy. *Chem. Mater.* **2016**, *28*, 6227–6232.

[189] Su, L. Z.; Wang, D. Y.; Wang, S. N.; Qin, B. C.; Wang, Y. P.; Qin, Y. X.; Jin, Y.; Chang, C.; Zhao, L. D. High thermoelectric performance realized through manipulating layered phonon-electron decoupling. *Science* **2022**, *375*, 1385–1389.

[190] Yang, L.; Chen, Z. G.; Han, G.; Hong, M.; Zou, Y. C.; Zou, J. High-performance thermoelectric $Cu_2Se$ nanoplates through nanostructure engineering. *Nano Energy* **2015**, *16*, 367–374.

[191] Ducka, A.; Trawiński, B.; Bochentyn, B.; Dubiel, A.; Kusz, B. Structure and thermoelectric properties of nickel-doped copper selenide synthesised in a hydrogen atmosphere. *Mater. Res. Bull.* **2021**, *133*, 111042.

[192] Li, J. Q.; Liu, F. S.; Ao, W. Q.; Hu, L.P.; Zhang, C. H. Improvement of the thermoelectric properties of GeTe- and SnTe-based semiconductors aided by the engineering based on phase diagram. *Int. J. Mater. Res.* **2022**, *113*, 340–350.

[193] Hong, M.; Zou, J.; Chen, Z. G. Thermoelectric GeTe with diverse degrees of freedom having secured superhigh performance. *Adv. Mater.* **2019**, *31*, 1807071.

[194] Li, J.; Zhang, X. Y.; Lin, S. Q.; Chen, Z. W.; Pei, Y. Z. Realizing the high thermoelectric performance of GeTe by Sb-doping and Se-alloying. *Chem. Mater.* **2017**, *29*, 605–611.

[195] Hong, M.; Chen, Z. G.; Yang, L.; Zou, Y. C.; Dargusch, M. S.; Wang, H.; Zou, J. Realizing zT of 2.3 in $Ge_{1-x-y}Sb_xIn_yTe$ via reducing the phase-transition temperature and introducing resonant energy doping. *Adv. Mater.* **2018**, *30*, 1705942.

[196] Zhang, X. Y.; Bu, Z. L.; Lin, S. Q.; Chen, Z. W.; Li, W.; Pei, Y. Z. GeTe thermoelectrics. *Joule* **2020**, *4*, 986–1003.

[197] Wang, D. Z.; Liu, W. D.; Li, M.; Yin, L. C.; Gao, H.; Sun, Q.; Wu, H.; Wang, Y. F.; Shi, X. L.; Yang, X. M. et al. Simultaneously

achieving high ZT and mechanical hardness in highly alloyed GeTe with symmetric nanodomains. *Chem. Eng. J.* **2022**, *441*, 136131.

[198] Gelbstein, Y.; Davidow, J.; Girard, S. N.; Chung, D. Y.; Kanatzidis, M. Controlling metallurgical phase separation reactions of the Ge$_{0.87}$Pb$_{0.13}$Te alloy for high thermoelectric performance. *Adv. Energy Mater.* **2013**, *3*, 815–820.

[199] Zhang, X. Y.; Li, J.; Wang, X.; Chen, Z. W.; Mao, J. J.; Chen, Y.; Pei, Y. Z. Vacancy manipulation for thermoelectric enhancements in GeTe alloys. *J. Am. Chem. Soc.* **2018**, *140*, 15883–15888.

[200] Zheng, Z.; Su, X. L.; Deng, R. G.; Stoumpos, C.; Xie, H. Y.; Liu, W.; Yan, Y. G.; Hao, S. Q.; Uher, C.; Wolverton, C. et al. Rhombohedral to cubic conversion of GeTe via MnTe alloying leads to ultralow thermal conductivity, electronic band convergence, and high thermoelectric performance. *J. Am. Chem. Soc.* **2018**, *140*, 2673–2686.

[201] Li, S.; Li, X. F.; Ren, Z. F.; Zhang, Q. Recent progress towards high performance of tin chalcogenide thermoelectric materials. *J. Mater. Chem. A* **2018**, *6*, 2432–2448.

[202] Du, B. S.; Jian, J. K.; Liu, H. T.; Liu, J.; Qiu, L. Recent advances in non-Pb-based group-IV chalcogenides for environmentally-friendly thermoelectric materials. *Chin. Phys. B* **2018**, *27*, 048102.

[203] Li, Y.; Shi, X.; Ren, D. D.; Chen, J. K.; Chen, L. D. Investigation of the anisotropic thermoelectric properties of oriented polycrystalline SnSe. *Energies* **2015**, *8*, 6275–6285.

[204] Li, C. W.; Hong, J.; May, A. F.; Bansal, D.; Chi, S.; Hong, T.; Ehlers, G.; Delaire, O. Orbitally driven giant phonon anharmonicity in SnSe. *Nat. Phys.* **2015**, *11*, 1063–1069.

[205] He, X. Y.; Zhang, H. Y.; Nose, T.; Katase, T.; Tadano, T.; Ide, K.; Ueda, S.; Hiramatsu, H.; Hosono, H.; Kamiya, T. Degenerated hole doping and ultra-low lattice thermal conductivity in polycrystalline SnSe by nonequilibrium isovalent Te substitution. *Adv. Sci.* **2022**, *9*, 2105958.

[206] LeBlanc, S.; Yee, S. K.; Scullin, M. L.; Dames, C.; Goodson, K. E. Material and manufacturing cost considerations for thermoelectrics. *Renew. Sustainable Energy Rev.* **2014**, *32*, 313–327.

[207] Yadav, G. G.; Susoreny, J. A.; Zhang, G. Q.; Yang, H. R.; Wu, Y. Nanostructure-based thermoelectric conversion: An insight into the feasibility and sustainability for large-scale deployment. *Nanoscale* **2011**, *3*, 3555–3562.

[208] Park, K. C.; Madavali, B.; Kim, E. B.; Koo, K. W.; Hong, S. J. Studies on microstructure and thermoelectric properties of p-type Bi-Sb-Te based alloys by gas atomization and hot extrusion processes. *J. Electron. Mater.* **2017**, *46*, 2915–2920.

[209] Wu, H. J.; Zheng, F. S.; Wu, D.; Ge, Z. H.; Liu, X. Y.; He, J. Q. Advanced electron microscopy for thermoelectric materials. *Nano Energy* **2015**, *13*, 626–650.

[210] Sarbu, I.; Dorca, A. A comprehensive review of solar thermoelectric cooling systems. *Int. J. Energy Res.* **2018**, *42*, 395–415.

**Dr Jamal – Deen Musah**　Jamal – Deen Musah received his MSc in physics from the National University of Science and Technology, MISiS, Moscow, Russia, in 2017 and completed his PhD in thermoelectric materials in 2021 at the City University of Hong Kong, China. His doctoral work focused on isovalent doping in metal chalcogenide materials for enhancing thermoelectric performance. He is now a postdoctoral researcher at the Hong Kong Polytechnic University, conducting further experimental research on the thermoelectric properties of various semiconductor materials.



**Dr A. M. Ilyas**　Ilyas A. M. received his PhD in physics from the City University of Hong Kong in 2021. He is currently a postdoctoral fellow in the Hong Kong centre for cerebro-cardiovascular health engineering. His research interests focus on deep learning application in MRI imaging, nanomaterial synthesis and fabrication of biosensors and energy conversion devices.



**Dr Shishir Venkatesh**　Shishir Venkatesh received his PhD in Materials Science & Engineering from the City University of Hong Kong in 2019. Currently, he is working in a medical device startup company in the USA. His research interests include semiconductor materials for electrochemical sensor applications, device fabrication and functional polymer synthesis.



**Dr Solomon Mensah**　Dr Solomon Mensah received his B.Sc. in Computer Science and Statistics and MEng in Computer Engineering from the University of Ghana. He holds a PhD in Computer Science from the City University of Hong Kong. He is currently a Senior Lecturer with the Department of Computer Science, University of Ghana, and the department's Lead Coordinator for the Data Science & Big Data Analytics Research Lab. His main research interests include predictive modelling using Bellwether data, software effort estimation, self-admitted technical debt analysis, deep learning, and big data analytics. He has published papers in prestigious journals and conferences, including but not limited to IEEE Transactions on Reliability, TSE, JSS, IST, QRS, ICSE, ESEM, SEKE, and ASE.

**Professor Samuel Kwofie**     Prof Samuel Kwofie is a full professor in the Department of Materials Engineering, KNUST, Kumasi, Ghana. He holds a BSc. (HONS) in Materials Science and Engineering, KNUST (Kumasi, Ghana), an MSc. in Welding and Adhesive Bonding from Brunel University, UK, and a PhD in Applied Mechanics from the University of the Witwatersrand, Johannesburg, South Africa. His research interests are in Materials Science and Engineering, Mechanical Behaviour of Materials, Fatigue and Fracture, Failure Analysis, and Modeling and Simulation of materials behaviour.



**Professor Vellaisamy A. L. Roy**     Vellaisamy A. L. Roy is a Professor of Intelligent Systems at the James Watt School of Engineering, University of Glasgow, Scotland, UK. He has published over 200 articles in journals on the engineering of materials and electronic devices. His research interests are in the fields of intelligent devices and systems for sensing applications, wearable thermoelectric and piezoresistive devices, and neuromorphic devices. In addition, he has 21 US/International/Chinese patents. He received a gold medal for his "Sensor Platform" at the International Exhibition of Inventions Geneva 2019.
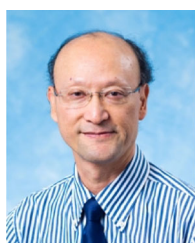


**Professor Chi-Man Lawrence Wu**     Prof Wu, currently a Professor at the Department of Materials Science and Engineering, City University of Hong Kong, China, obtained more than 60 research grants from various sources. Relating to research in computational materials science, he worked in areas of deformation of electronic interconnections, molecular mechanics and dynamics studies on composites, and density functional theory studies on energy, environmental, catalytic, chemical sensing and biosensing applications. He also works on biochemical sensing based on the localized surface plasmon resonance method and has successfully applied it to chemical, biological and medical diagnostic applications. For energy applications, the works are focused on topics such as thermoelectric power generation and hydrogen evolution reaction, using experimental investigations and various computational works.